Dynamics of recent landslides (

A. Guimpier, Susan J. Conway, A. Mangeney, A. Lucas, N. Mangold, M. Peruzzetto, M. Pajola, A. Lucchetti, G. Munaretto, T. Saemundsson, et al.

Dynamics of recent landslides (<20 My) on Mars: Insights from high-resolution topography on Earth and Mars and numerical modelling

A. Guimpier[1,2], S. J. Conway[1], A. Mangeney[3], A. Lucas[3], N. Mangold[1], M. Peruzzetto[3,4], M. Pajola[5], A. Lucchetti[5], G. Munaretto[5,6], T. Sæmundsson [7], A. Johnsson[8], L. Le Deit[1], P. Grindrod[9], J. Davis[9], N. Thomas[10], G. Cremonese[5]*

[1]*Laboratoire de Planétologie et Géodynamique, UMR6112 CNRS, Université de Nantes, France*

[2]*Université Paris-Saclay, France*

[3]*Université de Paris, Institut de physique du globe de Paris, CNRS, F-75005, Paris France*

[4]*Bureau de recherches géologiques et minières, Orléans, France*

[5]*INAF - Astronomical Observatory of Padova, Padova, Italy*

[6]*University of Padova, Padova, Italy*

[7]*University of Iceland, Reykjavík, Iceland*

[8]*University of Gothenburg, Gothenburg, Sweden*

[9]*Natural History Museum, United Kingdom*

[10]*University of Bern, Bern, Switzerland*

**corresponding author anthony.guimpier@univ-nantes.fr*

Keywords : Geomorphology – Digital Elevation Model – Landslides – Modelling – SHALTOP

Abstract

Landslides are common features found on steep slopes on Mars and the role of water in their formation is an open question. Our study focuses on three young martian landslides whose mechanism of formation is unknown and knowing their formation mechanism could give us key information on recent martian climate and/or tectonics. They are less than 5 km long, and formed during the Late Amazonian Epoch, with an age < 20 Ma when Mars is thought to have had a hyperarid climate. To better understand the dynamics and formation mechanism of these landslides, we combine two approaches: geomorphic comparison between martian and terrestrial landslides using remote sensing data from the High Resolution Imaging Science Experiment (HiRISE) and the Colour and Stereo Surface Imaging System (CaSSIS), and numerical modelling using a dry granular flow dynamical model. Our geomorphic analysis revealed two contrasting morphologies suggesting differing dynamics and formation mechanisms. Two of the three martian landslides resemble terrestrial rockslides, while the third is more akin to terrestrial mudslides. The numerical modelling, although not fully conclusive, broadly supports our interpretations from the morphological observations. We suggest that the two landslides resembling terrestrial rockslides could have been triggered by shaking by meteorite impact or marsquakes in the absence of water. On the contrary, we suggest liquid water (originating from ground-ice melted by geothermal heat flux) may have been involved in the initiation of the landslide resembling a terrestrial mudslide. Our results show the value of using morphological comparison between martian and terrestrial landslides combined with numerical modelling to inform the hypotheses of landslide-formation on Mars where in situ analysis is not usually possible.

1. Introduction

Large landslides were first observed on Mars in 1972 by the Mariner 9 probe, in Valles Marineris (Sharp, 1973). This region is characterised by a succession of steep-sided canyons, trending East-West over ~4000 km (Quantin et al., 2004a; Lucas et al., 2011; Brunetti et al., 2014; Watkins et al., 2015), with more than 1400 landslides (Crosta et al., 2018) formed between Hesperian (3.5 Ga) and Late Amazonian (50 Ma) (Quantin et al., 2004b). Several studies have investigated the morphology of the large landslides in Valles Marineris (Lucchitta, 1979; Quantin et al., 2004a; Soukhovitskaya and Manga, 2006; Brunetti et al., 2014; Crosta et al., 2018), which are characterised by scarps up to several kilometres wide and kilometre-deep, broad fan-shaped deposits, often wider than the scars from which they originated. The role that water may have played in these landslides is the main preocupation of these previous works and is important to understand because these landslides have occurred throughout Hesperian to Late Amazonian epochs so can provide information on Mars' climate through time. Mass movements can also give information on the tectonic history of a planetary body (Quantin et al., 2004b). The majority of previous studies of martian landslides have examined landslides with volumes greater than 10^{10} m^3, which is larger than landslides most commonly found on Earth. This lack of a direct terrestrial analogue is one of the reasons that the triggering and dynamics of these large landslides is still a subject of active research and the role of water and/or active tectonics is unclear.

To our knowledge, no studies have specifically focussed on understanding 'small' martian landslides with a volume less than 10^{10} m^3, which have a similar scale to landslides that can be found on Earth. These common terrestrial landslides are well-studied and their formation mechanisms are better understood than that of their larger counterparts. This provides an opportunity to perform a comparative morphological study between terrestrial analogues and martian landslides without the

need for scaling. We selected three relatively fresh, recent martian landslides (with potentially contrasting formation mechanisms), with the least influence of secondary processes on their surfaces (e.g., impact craters, aeolian features) and topographic data available, in order to increase the reliability and robustness of the comparative study. By identifying similar morphologies in the martian landslides and in terrestrial analogues, whose formation process is known, we can infer the processes that may have been at work on Mars.

In addition to this comparative morphological study, we use the thin-layer numerical code SHALTOP to simulate the landslide dynamics, assuming it is a dry granular flow. In spite of their simplifying assumptions and the uncertainty on initial and boundary conditions (see Section 2.3, and Delannay et al., 2017), thin-layer numerical models have previously been successful in reproducing the runout and approximate deposit morphology for a wide range of landslides on Earth and Mars. Using seismic data to reconstruct the dynamics of some terrestrial landslides, it was shown that thin-layer models can also reproduce these dynamics (Moretti et al., 2012, 2020; Levy et al., 2015; Yamada et al., 2016, 2018).

We therefore employ a double approach, using both morphological and numerical methods, to better constrain the mechanism of formation of these 'small' martian landslides and to understand their dynamics and hence, the potential role of liquid water and/or active tectonics.

First, in Section 2, we describe the data and the methods used to carry out this study, including the morphological analysis, age-estimation using crater size-frequency analysis and the numerical model used to carry out the simulations. In Section 3, we present the results from the morphological analysis, age estimation and numerical simulations. In Section 4 we first compare our results with those for other martian landslides presented in the literature, then discuss the potential emplacement mechanisms of the martian landslides and finally we assess the likelihood of the different hypotheses that could explain the formation of these three martian landslides.

2. Methodology

In this section, we elaborate the data and methods used to carry out the geomorphological analyses of the martian and terrestrial landslides. We also describe the crater counting method used to estimate the age of formation of martian landslides and then the method used to perform the numerical modelling.

2.1. Geomorphological analysis

In order to analyse the geomorphology of the martian and terrestrial landslides, we made measurements using the tools provided by the ArcGIS software. We first detail the data that we used during this study, then the analysis methods used for the martian and terrestrial landslides.

2.1.1. Datasets for martian landslides

We analysed the martian landslides at two scales: 1:1,000,000 scale for the geographical and geological context, and 1:4,000 scale to identify the key geomorphological structures. The analysis was performed in sinusoidal projection respectively centred at 325 °E, 322 °E and 78 °E for the Capri Chasma, Chryse Chaos and Nilosyrtis Mensae landslides.

At 1:1,000,000 we used the published geological and structural maps of Mars (Tanaka et al., 2014) and the Mars Orbiter Laser Altimeter (MOLA) Digital Elevation Model (DEM), with a resolution of

463 m/pixel (Smith et al., 2001). We used images from ConTeXt imager (CTX, Malin et al., 2007) onboard the Mars Reconnaissance Orbiter (MRO) with a resolution of ~6 m/pixel and from the Colour and Stereo Surface Imaging System (CaSSIS, Thomas et al., 2017) onboard the Trace Gas Orbiter (TGO) with a resolution of 4 m/pixel.

For the 1: 4,000 scale analysis we used images from MRO High Resolution Imaging Science Experiment (HiRISE, McEwen et al., 2007) with a resolution of 25 to 50 cm/pixel. We also used DEMs with a resolution of 2 m/pixel produced from HiRISE stereo observations using the Ames Stereo Pipeline (Moratto et al., 2010). These were vertically controlled to ESA's Mars Express High Resolution Stereo Camera (HRSC, Neukum and Jaumann, 2004) publically available DEMs.

Finally, near the Nilosyrtis Mensae landslide we made additional analyses of surface composition using Compact Reconnaissance Imaging Spectrometer (CRISM, Murchie et al., 2007) with a spatial resolution of ~19 m/pixel (*see supplementary material, S1- Spectral analysis*).

2.1.2. Datasets for terrestrial landslides

We used three terrestrial analogues, comprising landslides located near Abisko in Sweden, near Seattle in the USA and near Hólmavík in Iceland. We chose these three landslides because of their similar morphology to the martian landslides studied here. The dynamics and formation of terrestrial landslides is better understood than those on Mars, hence comparison between martian and terrestrial landslides is intended to provide additional information on the dynamics of the formation of the martian landslides of our study. We therefore used a similar resolution of data as for the martian landslides.

For the landslide located near Abisko in Sweden at 68°12' N, 19°2' E, a 2 m/pixel DEM derived from airborne laser altimetry was provided by the Swedish Land Survey, Geographical Sweden Data (GSD)-Elevation Data. For the landslide located near Seattle and Mount Rainier in Washington State in the USA at 46°59' N, 121°40' W, a 3 m/pixel DEM was used as provided by the Washington Lidar Portal (https://lidarportal.dnr.wa.gov). For the landslide located near Hólmavík in Iceland (65°42' N, 21°42' W), we used archived aerial images from the Land Survey of Iceland (LMI) at 30 cm/pixel and control points derived from the ArcticDEM (Porter et al., 2018) to reconstruct the topography using the commercial software AgiSoft Photoscan multiview photogrammetry resulting in a final DEM with a ground sampling of 60 cm/pixel.

2.1.3. General analysis

1:1M-scale analysis. At this scale we identified the presence or absence of similar landslides in the area surrounding our studied landslides. This scale also allowed us to identify faults and impact craters surrounding our landslides. Using the geological map of Tanaka et al. (2014) we were able to identify the units in which our landslides are located.

1:4k-scale image analysis. At this scale HiRISE images were used. We determined the size of the boulders (we use the term 'block' to refer to clasts > 4 m in length; Blair and McPherson (1999)) on the landslide deposits by measuring the long and short axes in planview and did not include the shadow. We made visual observations on the texture of the landslide deposits at the metre-length scale (e.g., rough, smooth, ripples) and made a visual assessment of the density of blocks on each landslide. To determine the height of the small structures, such as ridges, we extracted perpendicular topographic cross sections from the DEMs.

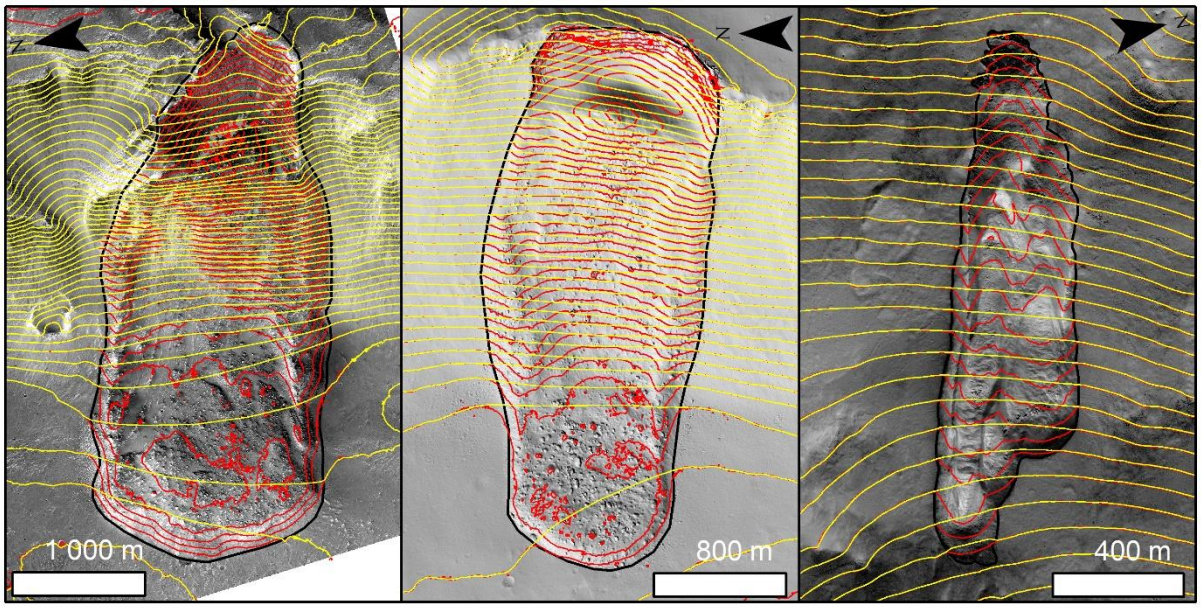

Figure 1 – Contour lines in red are derived from the original HiRISE DEM of each martian landslides of this study and contour lines in yellow are estimated pre-landslide contours. All these contour lines have an interval of 25 meters. (a) Capri Chasma landslide, CCh, HiRISE: ESP_035831_1760; (b) Chryse Chaos landslide, ChrC, HiRISE: PSP_005701_1920; (c) Nilosyrtis Mensae landslide, NM, HiRISE: ESP_027480_2075. Credits NASA/JPL/UofA.

Topographic reconstruction. In order to understand the spatial distribution of erosion and deposition, we generated a thickness map for each of the landslides. We had to make a reconstruction of the initial topography before the landslide occurred because no data are available from before the landslides formed. We took the difference between the reconstructed topography and the observed topography to generate the thickness map.

We estimated the initial topography by adapting the procedure described in Conway and Balme (2014) and de Haas et al. (2015) and took as guide the existing topography (Lucas and Mangeney, 2007; Lucas et al., 2011, 2014; Conway and Balme, 2014; Coquin et al., 2019). We used the DEMs to derive elevation contours for our landslides at 25 m intervals. We digitised the landslide boundary using slope and slope-aspect maps (derived from the DEM), as well as orthoimages. Slopes were calculated in each DEM cell as the average slope in a 3 × 3 cells neighbourhood around the central cell. The normal to the plane returns the aspect of the central cell. We then manually drew pre-landslide 'reconstructed' contours within the landslide boundary. We used the contours outside the landslide to guide our placement of the reconstructed contours and connected them manually to the two intersections of each contour line with the landslide boundary with a smooth curve, as shown in *Figure 1*.

The boundary line of the landslide was converted to point features at 2 m intervals and attributed with the elevation values of the DEM. The reconstructed contours in turn were converted to point features at 2 m intervals, attributed with the contour elevation value. These point features and associated elevations were then gridded into a 'reconstructed DEM' using the ArcGIS Natural Neighbour interpolation algorithm. The difference between this reconstructed DEM and the original DEM results in a thickness map, with positive values indicating areas of deposition and negative values indicating erosion. This reconstruction was also used to estimate the volume of deposition zone of the landslide. We summed the pixels with positive values and multiplied by the pixel size in the deposition zone to get an estimation of the deposition volume.

Landslide morphometrics. We used the thickness map to divide the landslides into erosion, transport and deposition "zones". The "erosion zone" is where the thickness map has predominantly negative values across the whole width of the landslide, the "transport zone" is where both positive and negative values are found across the width and where predominantly positive values are found across the whole width, this corresponds to the "deposit zone". We measured the maximum width of each of the zones perpendicular to the general slope of the surrounding escarpment and their length parallel to the general slope. We calculated the aspect ratio of the erosion zone by taking the ratio of its width to its length. We calculated the area by delimited the landslide boundary line by summing the number of DEM pixels within it and multiplying by their area.

Topographic profile analysis: We extracted two types of topographic profiles to derive additional morphometric characteristics: i) longitudinal profiles along the full length of the landside and ii) profiles at selected key positions within and outside the landslide.

We used the longitudinal profiles to analyse the variations in elevation and slope angle (computed with a 20 point running mean) within the landslide. We placed a topographic long profile along the centre of the landslide extending from ~60 m above the scar to ~60 m below the toe of the deposits. We used the same topographic long profile to calculate Heim's ratio which is the ratio between the total drop height *H* and the runout distance *ΔL',* both measured from the top of the scar to the toe of the deposit. This ratio has been previously calculated for martian and terrestrial landslides in the literature (Legros, 2002; Quantin et al., 2004a; Lucas et al., 2014; Brunetti et al., 2014; Crosta et al., 2018) and is used to assess the mobility of a mass movement. The lower the ratio is, the longer the runout of the landslide is compared to the drop height and the greater its mobility.

Three topographic profiles were extracted for the levees, the steepest parts of the erosion zone, the transport zone and the front scarp (see *Figure S2* in the supplementary material for the precise position of these topographic profiles for each landslide). The cross-section along levees are used to compute the height and width of each levee, as well as the slope between the base and the crest of the levee.

For the steepest part of the erosion zone, we placed three profile lines in the centre and at the edges of the erosion zone perpendicular to the contour lines. For the transport zone three profiles were placed perpendicular to the contour lines at horizontal intervals of between 200 and 300 metres. For the front scarp one profile was placed in the central part and two near the edges of the front scarp. These profiles were used to calculate the average slope of these features.

We extracted one elevation profile ~300 m outside the boundary landslide (*Figure S2*), and perpendicular to the contour lines, in order to estimate the slope angles of the terrain before the landslide occurred and the slope angle of the deposit zone. This profile extended from the top to the bottom of three zones defined above. Here we take only one profile, because the further profiles are placed from the landslide, the less likely they are to be representative of the pre-landslide surface. For each zone we calculated the slopes, with the methodology as described above.

For each zone of the landslide, we report the means and ranges of the slope values calculated from the profiles.

2.2. Age estimations of martian landslides

In order to estimate when the martian landslides formed, we used the crater size-frequency distribution method to obtain model ages. We used ArcGIS CraterTools (Kneissl et al., 2011) and

Craterstats2 (Michael and Neukum, 2010; Michael et al., 2012). This method exploits models which describe how the bolide production function varies over time, enabling the size-frequency distribution of impact craters present on a planetary surface to be linked to a modelled surface age (Michael and Neukum, 2010; Michael et al., 2012; Michael, 2013; Michael et al., 2016).

In the deposition zone (described in section 2.1), we digitized craters to compute their distribution in size. The deposit zone area and the size-frequency distribution of the superposed craters are then used as inputs for Craterstats2 (Michael and Neukum, 2010; Michael et al. 2012). Due to the small surface area of the landslides studied here and the low number of impact craters on their surface, there are large margins of error in these estimations (e.g., Warner et al., 2015).

2.3. Numerical modelling

Numerical modelling has already been successfully used to better understand landslides on Mars and compare them with terrestrial ones (Soukhovitskaya and Manga, 2006; Lucas and Mangeney, 2007; Mangold et al., 2010; Lucas et al., 2011, 2014). Following previous work (Lucas and Mangeney, 2007; Lucas et al., 2011, 2014; Brunet et al., 2017), we model our martian landslides with the numerical code SHALTOP and compare the simulation results with the observed deposits.

2.3.1. Model input preparation

In SHALTOP simulations, the topography on which the modelled landslide propagates is the reconstructed topography (*see section 2.1.3*), but with only the deposits removed, and the erosion zone remains unchanged – we call this the "scar topography" to differentiate it from the reconstructed topography described above. The initial mass is given by the difference between the reconstructed topography and the scar topography (Fig.2). Reconstruction of the topography and of the initial mass is challenging and can significantly affect the results (Lucas et al., 2011; Moretti et al., 2015; Peruzzetto et al., 2019).

We smoothed the reconstructed topography twice to remove small artefacts related to the reconstruction method (e.g., subtle elevation steps at the landslide boundary). In the first pass, we calculated the mean elevation value within a 10-pixel square moving window. In the second, we calculated the mean value within a 6-pixel radius circular moving window. In order to avoid overestimating the travel distances produced in the model, we added back roughness after smoothing, as follows. First we chose a typical sample area of the terrain outside the landslide of the same size as the landslide itself. We smoothed the elevation data within the terrain sample by averaging the elevation values within a moving window 10 × 10 pixels in size and applied this procedure three times. We differenced this smoothed sample with the original to obtain a DEM with only the meter-scale roughness (because of the DEM vertical resolution), which was then added to the landslide zone.

2.3.2. Model evaluation and analysis criteria

The first criterion used to compare our simulations to observations is the runout distance. We also considered two secondary criteria: the final position of the centre of mass and the deposit thickness map (*see section 2.1.3*), to assess the simulation results. To calculate the centre of mass, we first extracted the positive values of the thickness map corresponding to the deposits of each landslide. A grid of deposit thicknesses is a direct output of the model so no extraction is required. Then we convert the deposition thickness map into points where each point corresponds to a pixel and contains its

thickness value. The *x* and *y* coordinates of the centre of mass is calculated according to the average *x* and *y* coordinates of the centroids of each point weighted by the thickness value.

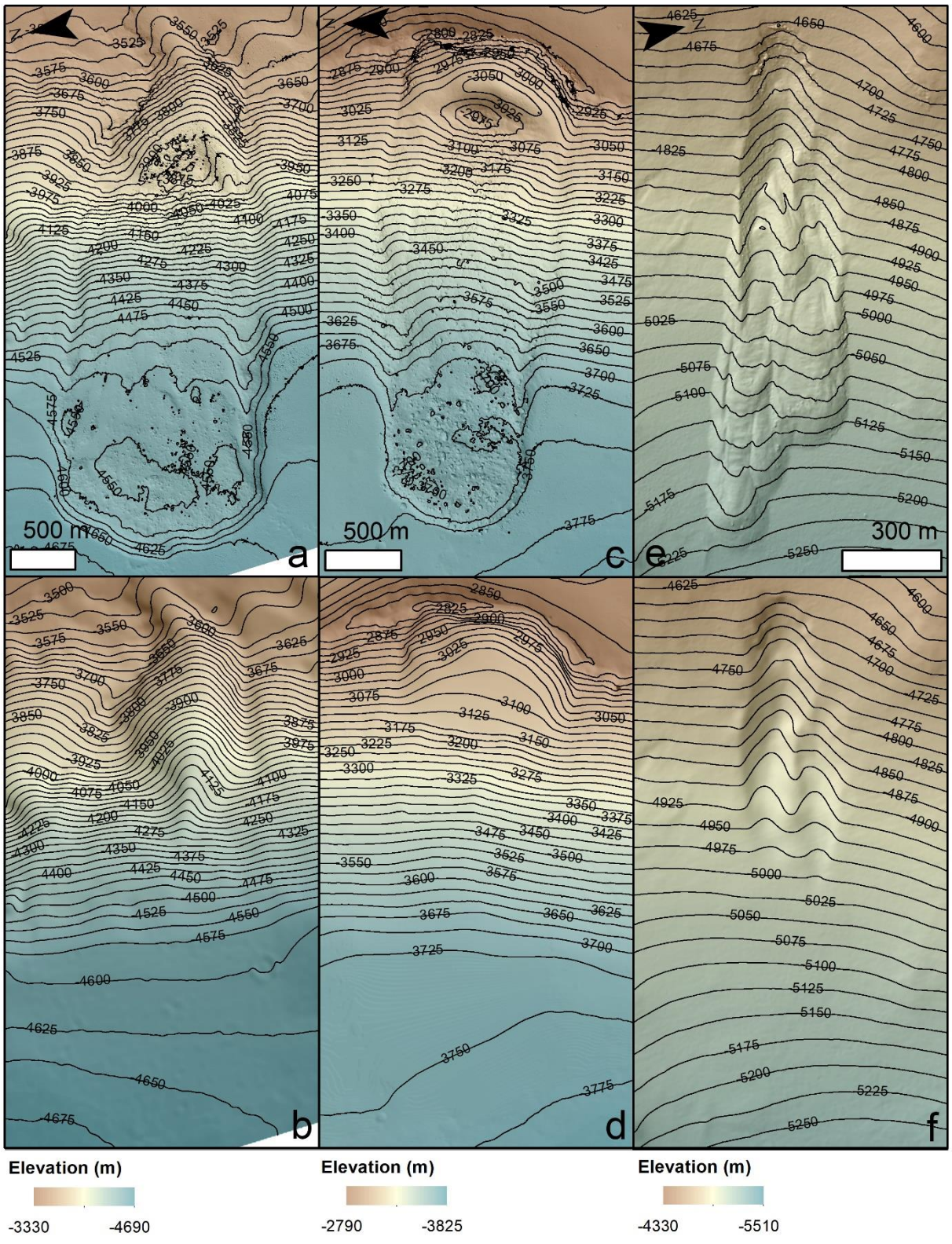

Figure 2 - A 3D shaded-relief rendering of the Capri Chasma (CCh, a & b); Chryse Chaos (ChrC, c & d) and Nilosyrtis Mensae (NM, e & f) with their respective topography. (a, c, e) Is the present-day topography. (b, d, f) Is the topographic input for SHALTOP, where the estimated pre-landslide surface is combined with the present-day erosion zone.

2.3.3. SHALTOP description

SHALTOP is a numerical model that simulates homogeneous flows propagating on complex topography using the thin-layer approximation (that is, simplifications to the governing equations that can be used when the flow thickness is small in comparison to its lateral extent) (Bouchut et al., 2003; Bouchut and Westdickenberg, 2004; Mangeney-Castelnau et al., 2005; Mangeney et al., 2007). In the thin-layer approximation, the flow is described by its thickness h in the direction normal to the topography and by its depth-averaged velocity u. In SHALTOP, energy is dissipated through basal friction. In contrast to most of the depth-averaged landslide models, SHALTOP accounts for the curvature tensor of the topography with all its components. The resulting topography effects can significantly change the runout and/or flow velocity, in particular for rapid granular flows over complex topographies (Peruzzetto et al., 2020). SHALTOP has already been used to successfully model terrestrial landslides (Lucas et al., 2007; Favreau et al., 2010; Moretti et al., 2012, 2015, 2020; Brunet et al., 2017; Yamada et al., 2016, 2018; Peruzzetto et al., 2019), as well as martian landslides and recent gullies (Mangold et al., 2010; Lucas and Mangeney, 2007; Lucas et al., 2011, 2014). We recognise that thin-layer models lack some of the features of real flows such as the presence of water, erosion/deposition processes or polydispersity (particles with very different sizes) (Delannay et al., 2017). However, our knowledge of the model limitations, in particular when compared to granular experiments (Mangeney-Castelnau et al., 2005; Mangeney et al., 2007; Gray, 2014; Rocha et al., 2019) makes it possible to better interpret the comparison between simulated and observed deposits.

In the simplest Coulomb friction law implemented in SHALTOP, the friction coefficient μ, is constant during the simulation. Using SHALTOP to simulate about 15 landslides on Earth and Mars, Lucas et al. (2014) found that the coefficient of friction decreases with increased volume of material released during these landslides due to the increase of the flow velocity. As a result, there is a relationship between the volume of the landslide and the friction coefficient associated with its movement. The friction coefficient therefore also varies as a function of the landslide runout distance.

In our investigation, we will vary this friction parameter to best-fit runout distance, and then compare the results to the empirical law of Lucas et al. (2014) $\mu = V^{-0.0774}$ where V is the landslide volume.

Laboratory experiments show that μ may actually depend on the flow velocity and thickness.

Hence, we will also use the Pouliquen and Forterre friction law (Pouliquen and Forterre, 2002) to simulate our landslides in the SHALTOP model. This law involves six empirical parameters: three friction angles, $\delta_{1,2,3}$, the particle size, L, an empirical dimensionless parameter, β (deduced from laboratory experiments and taken as constant here (β= 0.136)), and an exponent γ (γ= 10^{-3}).

Several regimes, low-velocity and high-velocity, are described depending on the Froude number (*Fr*) defined as $\frac{u}{\sqrt{gh}}$.

If $F_r \geq \beta$

$$\mu(h,u) = \tan\delta_1 + (\tan\delta_2 - \tan\delta_1)\frac{1}{1+\frac{\beta h\sqrt{gh}}{L\ u}} \quad (1),$$

If $F_r = 0$

$$\mu(h) = \mu_{start}(h) = \tan\delta_3 + (\tan\delta_2 - \tan\delta_1)\frac{1}{1+\frac{h}{L}} \quad (2),$$

If $0 \leq F_r \leq \beta$

$$\mu(h,u) = \mu_{start}(h) + \left(\frac{F_r}{\beta}\right)^{\gamma}\left(\mu_{stop}(h) - \mu_{start}(h)\right) \quad (3),$$

Where

$$\mu_{stop}(h) = \tan\delta_1 + (\tan\delta_2 - \tan\delta_1)\frac{1}{1+\frac{h}{L}} \quad (4).$$

With the Pouliquen and Forterre law, when h decreases and u increases, μ increases and vice versa. $\mu_{stop}(h)$ and $\mu_{start}(h)$ represent the tangent of the slope angle required for a certain material thickness h to stop or start to flowing, respectively. In order to reduce the number of fitting parameters in the Pouliquen and Forterre friction law, we fix the dimensionless parameters β and γ as well as the difference δ_2 - δ_1 and δ_3 - δ_1. Thus the only parameters that will be fitted to match observed travel distances are δ_1 (with $\delta_2 = \delta_1 + 10°$ and $\delta_3 = \delta_1 + 2°$) and L (Brunet et al., 2017).

In the model, we used the acceleration due to gravity on Mars g = 3.73 m.s^{-2}. We used a maximum simulation duration of 1200 s, as after this time there was no further variation in both the velocity and thickness of the simulated flows. Fourteen tests were carried out (seven for each landslide for the two friction laws) in order to obtain the coefficients of friction that best reproduce the observed runout distance.

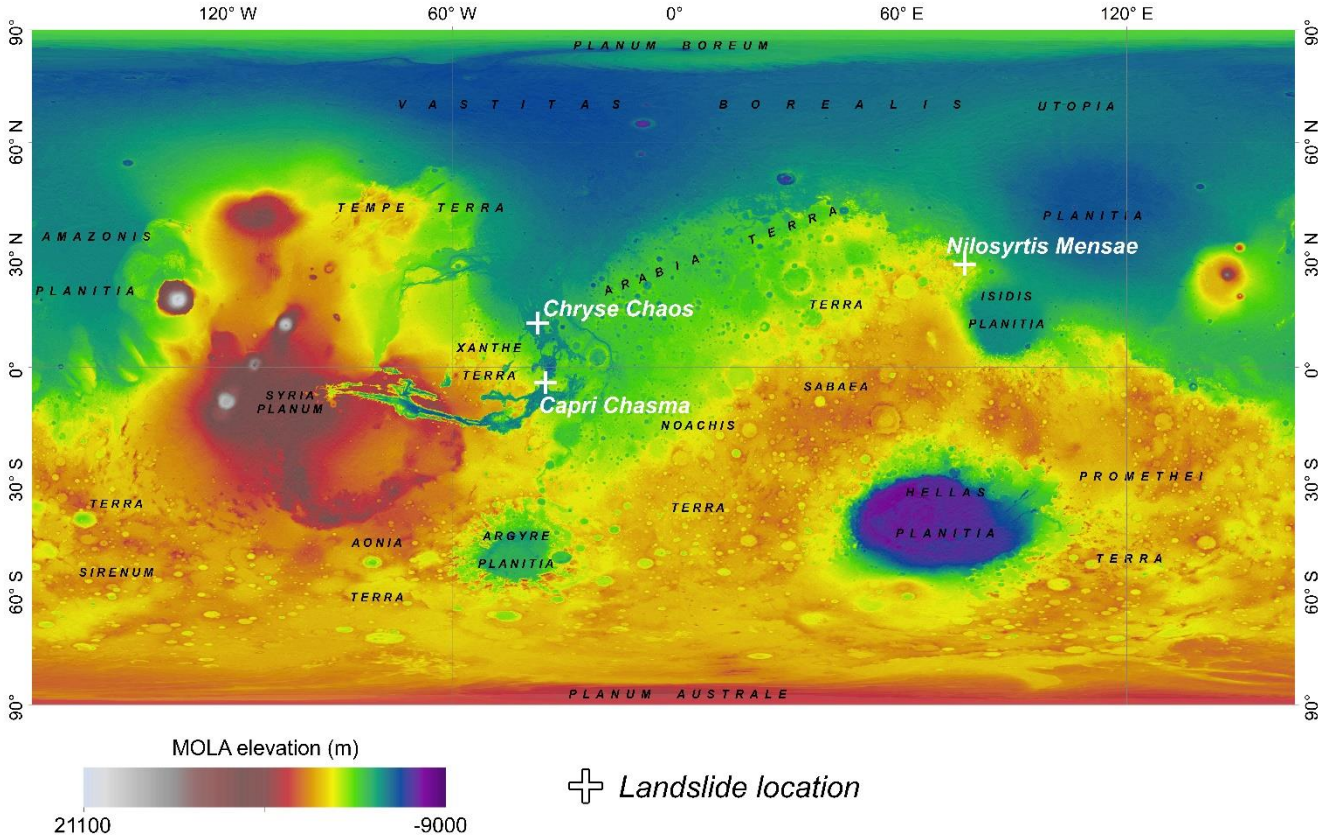

Figure 3 - Location of the three studied landslides on a colourised MOLA topographic map of Mars with semi-transparent shaded relief (Smith, et al., 2001).

3. Results

In this section we present the geomorphological results (Section 3.1), the age estimates (Section 3.2) and numerical modelling (Section 3.3). Section 3.1 is divided into two parts, the first concerning the description of the results for the martian landslides followed by a comparison to the terrestrial landslides.

3.1. Geomorphological results

3.1.1. Martian landslides

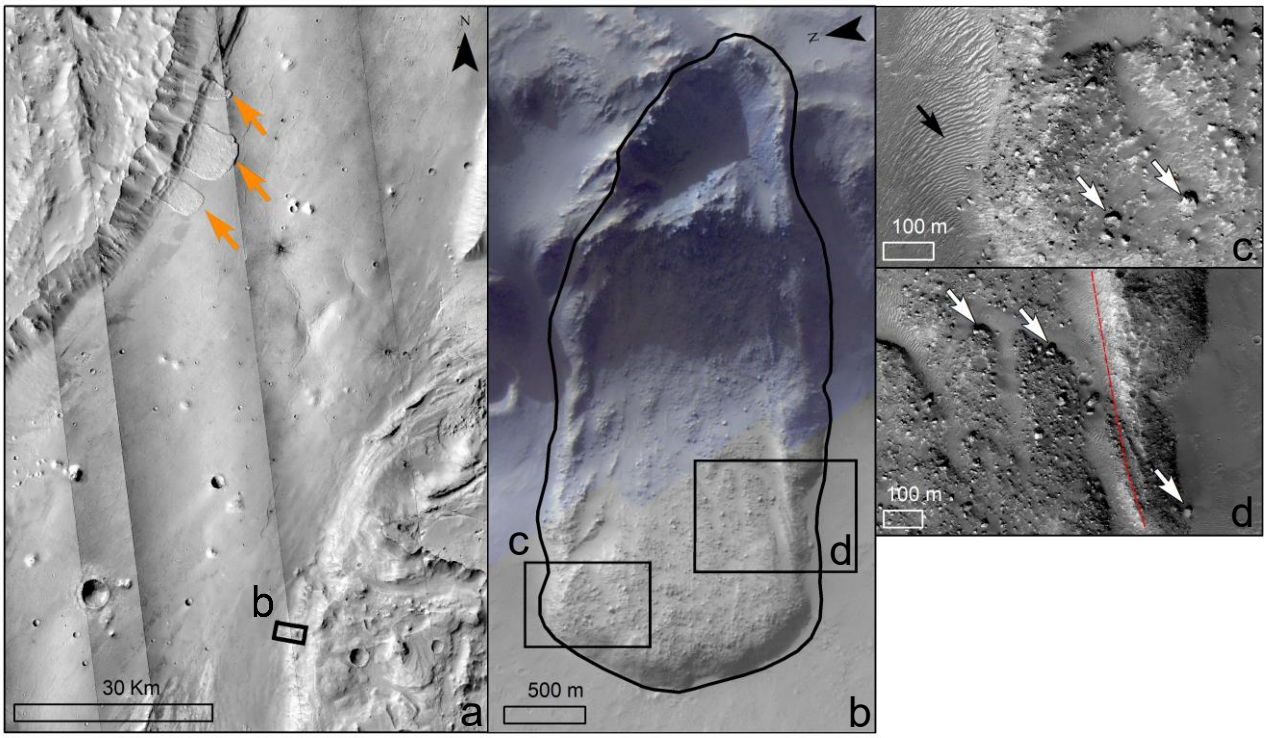

Figure 4 - The Capri Chasma (CCh) landslide. (a) Regional view of the area around the CCh landslide, which is outlined by the black rectangle indicating the location of panel (b), the orange arrows indicate three larger landslides located on the other side of the outflow channel. The background is a mosaic of CTX images P20_008707_1757, P07_003578_1757, G21_026271_1756, G03_019546_1753, and D06_029515_1755. (b) CaSSIS image of CCh landslide (MY35_008462_188, PAN-BLU filters). (c) & (d) Detailed view of the landslide deposit, black arrows indicate windblown deposits, white arrows indicate boulders more than 30 m in diameter, red dotted line indicates the inner edge of the southern lateral levee (HiRISE: ESP_035831_1760). Credits: NASA/JPL/UofA/MSSS/ESA/Roscosmos/UniBe.

Capri Chasma landslide. The Capri Chasma landslide (CCh) is located between Xanthe Terra and Margaritifer Terra, at 4°4' S, 35°2' W (*Fig.3*). The region around this landslide is dominated by a series of north-south trending canyons at the eastern extent of Capri Chasma, a canyon leading to the outflow channels named Tiu Valles downstream (Coleman et al., 2007) (*Fig.4a*). The landslide is located on the eastern flank of Capri Chasma on an escarpment which rises 2800 m above the canyon floor on the middle Noachian highland unit 'mNh', (see Tanaka et al., 2014). Tanaka et al. (2014) describe this unit as featuring degraded to severely degraded undifferentiated materials resulting from meteorite impacts, volcanic flows, and possibly sedimentary and fluvial deposits and is dated to between 4.5 and 3.7 billion years old.

The landslide faces west, measures ~4 km long and ~1.7 km-wide at its widest point. Its key attributes are summarised in *Table 1*. The arcuate landslide scar is characterised by a continuous well-defined

slope-break demarking the upper limit of the erosion zone (*Fig.5a, red dashed line*). The slopes in the erosion zone reach 52° at the scar itself, and gradually decrease in the downslope direction away from the scar. Below the scar, the erosion zone is dominated by a talus slope with metre-scale blocks. Downslope these blocks become mantled by aeolian deposits.

Martian Landslide		Capri Chasma (CCh)	Chryse Chaos (ChrC)	Nilosyrtis Mensae North Lobe (NM)	Nilosyrtis Mensae South lobe (NM)
Latitude		4°4’ S	11° 43’ N	27° 24’ N	
Longitude		35°2’ W	37° 6’ W	76° 42’ E	
Erosion zone	Maximum length (m)	1000	500	500	750
	Maximum width (m)	1080	1200	200	220
	Aspect ratio (length/width)	0.9	0.4	2.9	3.4
	Area (m²)	$1.4x10^6$	$1.0x10^6$	$6.4x10^4$	$1.2x10^5$
	Steepest slope (°)	52	70	40	
	Mean slope (°)	30	35	30	
Transport zone	Maximum length (m)	1350	1700	-	
	Maximum width (m)	1685	1350	-	
	Mean slope (°)	26	23	-	
	Mean adjacent slope (°)	25	23	25	
Deposit zone	Maximum length (m)	1620	1050	590	830
	Maximum width (m)	1700	1000	210	190
	Area (m²)	$3.2x10^6$	$2.0x10^6$	$1.2x10^5$	$1.7x10^5$
	Volume (m^3)	$1.4x10^8$	$4.0x10^7$	$2.1x10^6$	$2.4x10^6$
	Maximum thickness (m)	112	64	34	31
	Range (and mean) of front scarp angle (°)	21 – 27 (24)	19 – 24 (21)	27 – 32 (29)	27 – 28 (27.5)
	Mean adjacent slope (°)	1	3	20	
Levee	Mean height (m)	45	20	20	
	Range (and mean) of lateral angle (°)	9 - 15 (12)	8 - 10 (9)	22 - 30 (26)	23 - 25 (24)
Maximum boulder size (m)		40	60	10	

Table 1 – Summary of the morphological attributes of the martian landslides. Note that the value given in volume of the deposit zone, takes into account the volume found in the deposit zone plus the volume of the lateral levees located in the transport zone for ChC and ChrC.

At the base of the erosion zone, there is a slope reversal of ~18° where some of the failed material has remained (*Fig.5a, red dashed line*). This material has an angular texture similar to the material constituting the deposit further downslope.

Immediately below the main erosion scar, there is a transport zone with a slope of ~26° decreasing to 1° near the deposit zone (*Fig.5a, between blue and red dashed lines*). In this zone low lateral levees are

present (*Fig.5b, black arrows, Table 1*). This transport zone contains fewer blocks than the deposit zone.

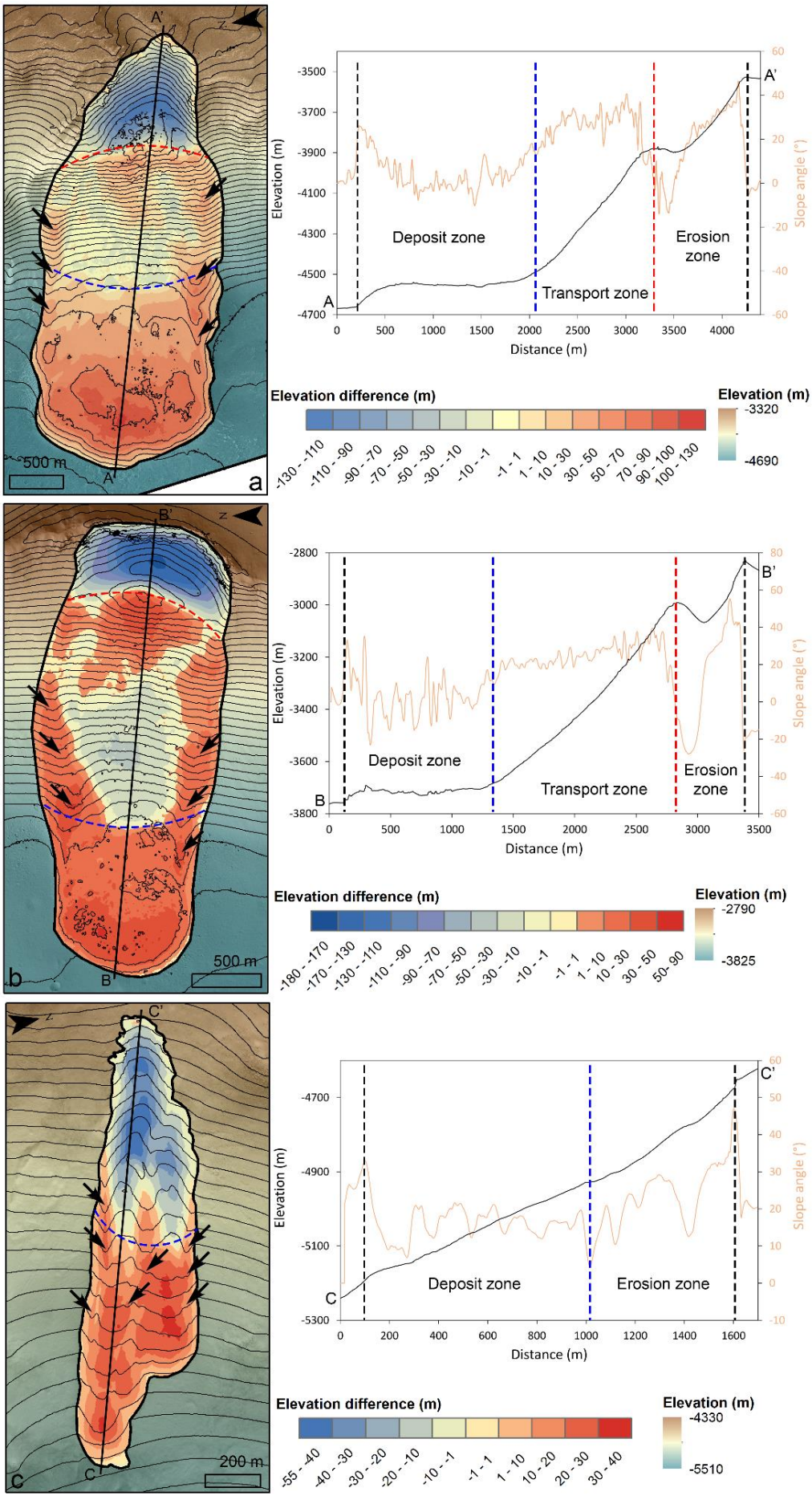

Figure 5 – Colourised digital elevation model with semi-transparent ortho-image overlain by elevation difference map, long profile and topographic contours with 25 m interval marked in black for (a) Capri Chasma CCh, A-A'; (b) Chryse Chaos ChrC, B-B' and (c) Nilosyrtis Mensae NM, C-C'. For each long profile plot the slope angle variation is indicated by the orange line. The dashed lines delimit the erosion, transport and deposition zones of the landslides. The black arrows indicate lateral levees. HiRISE images: (a) ESP_035831_1760; (b) PSP_005701_1920; (c) ESP_027480_2075. *Credit: NASA/JPL/UofA.*

The transport zone and the deposit zone that follows have similar width (*Fig.5a, blue dashed line, Table 1*). The deposit reaches a maximum thickness of 112 metres (*Fig.5a*). Where the deposit lies on flat ground, it forms a single steep-sided and flat-topped lobe with a thickness that increases gradually towards the toe. The texture of the deposition surface is rough and irregular. Several hundred blocks >10 m in diameter are distributed between the front of the deposit and at the base of the erosion zone (*Fig.4c & d).* Another concentration of blocks is found on the deposit that remains in the erosion zone, containing a block of 40 m in diameter. Some metre-scale aeolian bedforms are also observed at the toe of the deposit zone (*Fig.4c*).

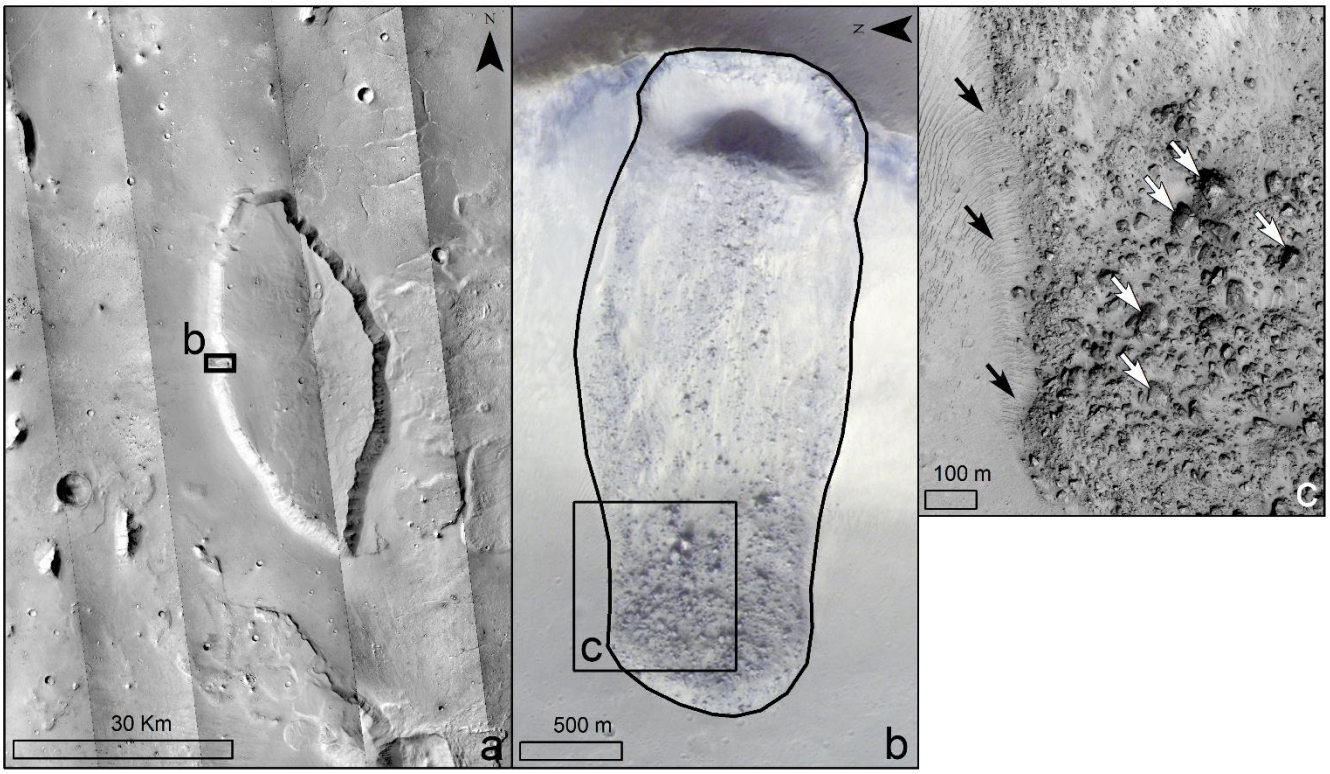

Figure 6 - The Chryse Chaos (ChrC) landslide. (a) Regional view of the area surrounding the ChrC landslide where the black rectangle indicates the position of the landslide and panel b. CTX images: D15_033207_1901, G20_026060_1913, P08_004145_1902, P17_007626_1902, and F03_036965_1906. (b) CaSSIS image of the ChrC landslide (MY35_010023_012, PAN-BLU filters). (c) Detailed view of the landslide deposit, black arrows indicate windblown deposits, white arrows indicate boulders more than 50 m in diameter (HiRISE image PSP_005701_1920). Credits: NASA/JPL/MSSS/UofA/ESA/Roscosmos/UniBe.

Chryse Chaos landslide. The Chryse Chaos landslide (ChrC) is located at 11°43' N, 37°6' W (*Fig.3*), in Simud Vallis, an outflow channel (Pajola et al., 2016) that together with Tiu Vallis is believed to have carried water flowing from Valles Marineris into the putative ocean of Chryse Planitia (Tanaka et al., 2003) (*Fig.6a*). Its key attributes are summarised in *Table 1*. Tanaka et al. (2014) report that this region is underlain by the 'Hto' unit, a transition valley unit dated to the Hesperian (3.56 – 3.24 Ga), composed of fluvial deposits from Tiu Vallis. Pajola et al. (2016) indicate four different evolutionary stages occurred in the area, including possible flow inversions and ponding. The landslide is located on the west-flank of a flat-topped mesa in the middle of the valley's floor rising up to 950 m above it. The mesa is composed of basement materials, with a modelled age that is Middle Noachian and consists of friable sediments, impact debris and volcanic material (Tanaka et al., 2014; Pajola et al., 2016).

The erosion scar of the ChrC landslide is well defined and, in some places, bedrock outcrops are apparent and several blocks seem to have detached from these outcrops. Below the scar, the erosion zone is characterised by a talus slope at ~35° with blocks visible at the base of the talus (*Fig.5b*) and is

relatively short compared to the total length of the landslide (*Fig.5b*; *Table 1*). As for the CCh landslide, the base of the erosion zone is characterised by a slope reversal of ~20° where deposits have remained (*Fig.5b, red dashed line*).

Downslope of the slope reversal there is the transport zone, characterised by slopes of approximately 23 °and lateral levees (*Fig.5b, black arrows, Table 1*). The transport zone width decreases from 1350 m to 920 m when the slope reaches 3° at the deposit zone. Then as for CCh landslide, the transport zone is followed by the deposit zone where the deposit forms a single steep-sided and flat-topped lobe. Its thickness gradually increases toward the toe to reach a maximum thickness of about 64 m (*Fig.5b*). We observe fluctuations in slope angle on the deposit zone that indicates a very high surface roughness, which can be explained by the presence of several dozen boulders of 60 m in diameter (*Fig.6c, white arrows*), also as for CCh, several hundred blocks >10 m in diameter are distributed between the front of the deposit and at the base of the erosion zone. We also observe some aeolian bedforms at the toe of the deposit (*Fig.6c, black arrows*).

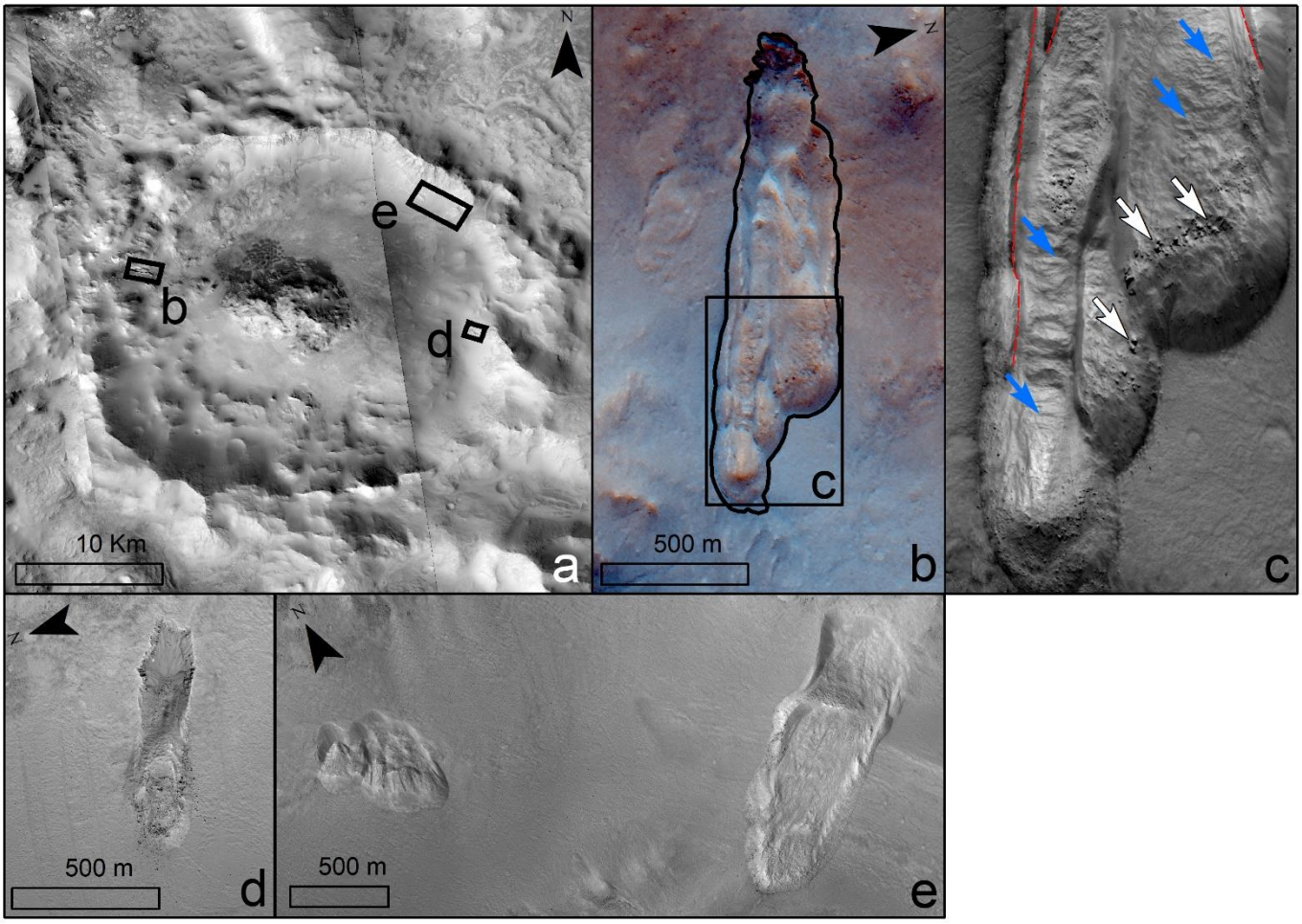

Figure 7 - The Nilosyrtis Mensae (NM) landslide. (a) Regional view of the area surrounding the NM landslide. Black rectangles indicate the positions of panels b, d and e. CTX images: D04_028680_2064, B16_015942_2088, B11_014109_2058, G01_018777_2091, G18_025225_2058, P06_003310_2082, and B03_010707_2080. (b) CaSSIS colour image of the Nilosyrtis Mensae landslide (MY35_008751_028, PAN-BLU filters). (c) Detailed view of the NM landslide in (b), where white arrows indicate boulders more than 5 m in diameter, and blue arrows indicate perpendicular ridges on the deposit (HiRISE: ESP_026781_2075). (d) & (e) Other landslides in same impact crater on HiRISE images ESP_053457_2075 & ESP_057110_2075, respectively. Credits: NASA/JPL/UofA/MSSS/ESA/Roscosmos/UniBe.

Nilosyrtis Mensae landslide. The Nilosyrtis Mensae (NM) landslide (*Fig.7b*) is located at 27°24' N, 76°42' E, 150 km to the north of the Nili Fossae, at the southwest margin of Utopia Planitia and southeast of Nilosyrtis Mensae on the western wall of a 25 km diameter and 1.7 km deep impact crater (*Fig.7a*). The crater is located within a transitional unit dated between the Noachian and the Hesperian (HNt), which is composed of Noachian impacts, sedimentary and volcanic deposits, and intervening aprons dated to the Hesperian (Tanaka et al., 2014). This region is characterised by the presence of tectonic grabens (the Nili Fossae) generated by a major fault system, probably related to the Isidis impact basin (Wichman and Schultz, 1989; Kraal et al., 1998). The region is also characterised by the presence of fluvial erosion and deltaic deposits which date back to the Late Noachian, between 3.85 to 3.7 Ga (Fassett and Head, 2005). In addition, phyllosilicates have also been reported in this region (Bibring et al., 2005; Poulet et al., 2005; Mustard et al., 2007; Mangold et al., 2007; Carter et al., 2013).

The NM landslide is located on a continuous slope inclined eastward at ~25° (*Fig.5c*), and has two main lobate structures (*Fig.7b*). A summary of the characteristics of both of these lobes can be found in *Table 1*. The landslide has an erosion and deposition zone, but does not show a distinct transport zone (*Fig.5c*).

Two erosion zones are present upslope of each lobate deposit with their interior slopes reaching a maximum value of 40°. There are tracks left by rolling blocks (e.g., Tesson et al., 2019), particularly in the southern erosion zone. No slope breaks are observed between the erosion zone and deposit zone (*Fig.5c*).

Lateral levees are present on the flanks of the landslide depositional lobes (*black arrows on Fig.5c, Table 1*). Levees on the southernmost lobe are more pronounced than those on the northern lobe (*Fig.5c)*. The deposits are also characterised by ridges perpendicular to the direction of flow, mainly present at the distal end of the landslide (*Fig.7c, blue arrows*). The average deposit thickness is ~30 m spread evenly over the whole deposit surface with a maximum thickness of ~34 m. Also, we were able to distinguish blocks of about 10 m in diameter at the front of the landslide deposition surface.

A similar lobate morphology is shown by three other smaller landslides within the same crater (*Figs.7d & e*). They are 1.6 km, 900 m and 500 m long, respectively and are present on a similar substrate, at a similar altitude as the landslide studied here.

3.1.2. Terrestrial landslides

To better understand the formation mechanism of martian landslides, we compare them to terrestrial analogues. The morphological description of the three martian landslides shows a clear morphological difference between the CCh and ChrC landslides and the NM landslide. For this reason, the description of terrestrial analogues has been subdivided into two different sections.

Capri Chasma and Chryse Chaos analogue. We compare here the CCh and ChrC landslides to a similar-looking landslide located in the Abisko region in Sweden at 68°12' N, 19°2' E. The landslide (*Fig.8a & b*) is classified as a rockslide by Rapp (1960). Rapp (1960) indicates that it is probably a post-glacial landslide because the rockslide deposit partly covers glaciofluvial deposits. Its formation has therefore been linked to the release of overburden pressure induced by the disappearance of the valley glacier. The measurements concerning the Abisko landslide are summarised in *Table 2*.

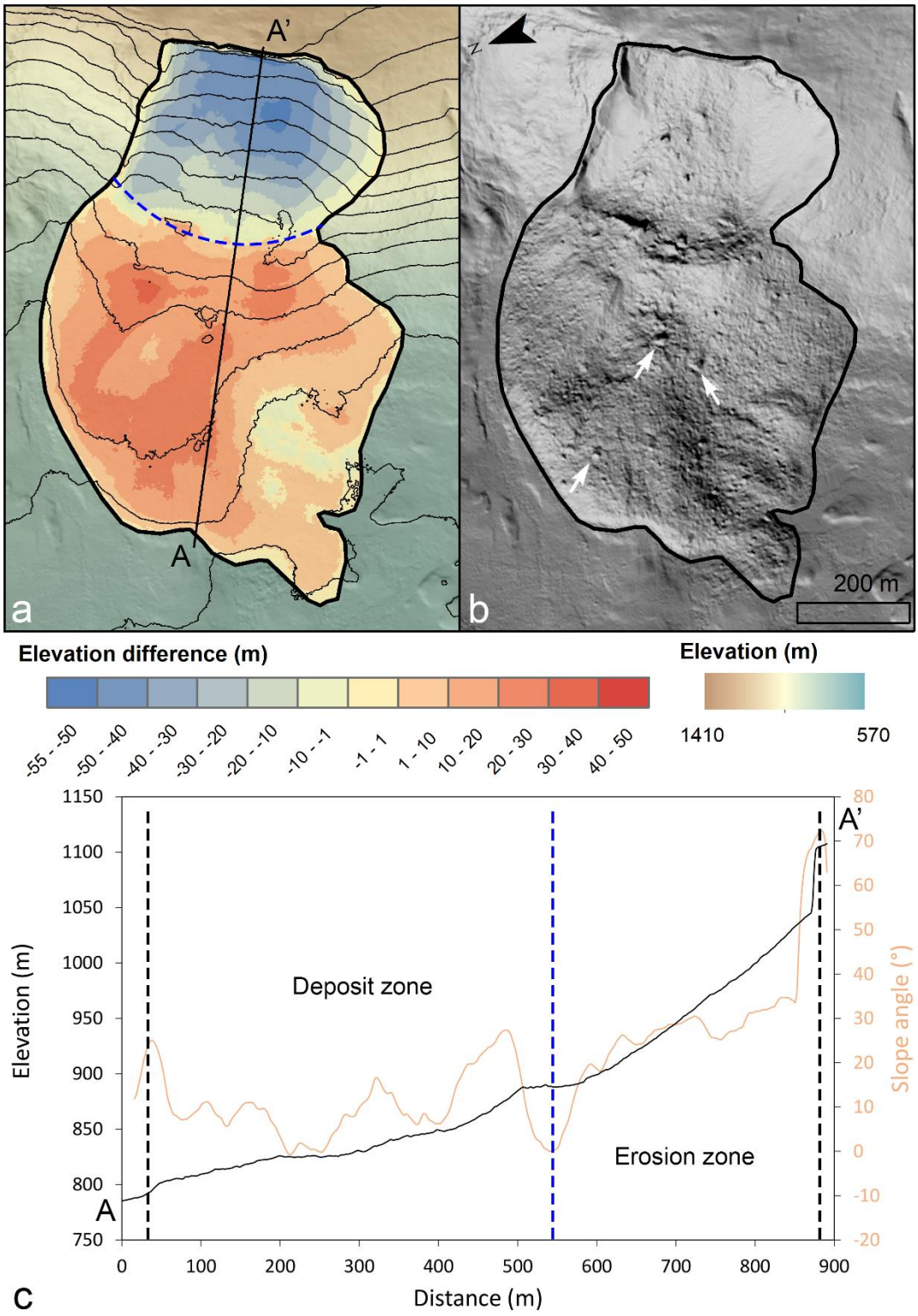

Figure 8 – The Abisko rockslide, Sweden. (a) Colourised digital elevation model with semi-transparent hillshaded relief overlain by elevation difference map and long profile derived from LiDAR topography for the Abisko landslide marked with the location of the long profile in panel c. Topographic contours with 25 m interval are marked in black. (b) LIDAR hillshaded relief image for the Abisko landslide, white arrows indicate boulders on the deposit. (c) Elevation profile and slope angle variation of the Abisko rockslide from A to A' in panel a, dashed lines indicate the erosion and deposit zones. Image credits: Geographical Sweden Data (GDS).

Terrestrial Landslides		Abisko	Hólmavík	Mount Rainier
Latitude		67°12' N	65°42' N	46°59' N
Longitude		19°2' E	21°42' W	121°40' W
Erosion zone	Maximum length (m)	340	340	550
	Maximum width (m)	440	150	350
	Aspect ratio (length/width)	0.7	2.2	1.5
	Steepest slope (°)	85	65	70
	Mean slope (°)	39	33	43
Transport zone	Maximum length (m)	-	100	-
	Maximum width (m)	-	140	-
	Mean slope (°)	-	11	-
	Mean adjacent slope (°)	27	15	24
Deposit zone	Maximum length (m)	519	295 - 320	435 - 470
	Maximum width (m)	510	150	350
	Area (m^2)	$1.2x10^6$	$5.7x10^4$	$1.6x10^6$
	Volume (m^3)	$3.5x10^6$	$3.3x10^5$	$2.2x10^6$
	Maximum thickness (m)	34	12	33
	Range (and mean) of front scarp angle (°)	14- 21 (17)	12 - 20 (17)	29 - 36 (32)
	Mean adjacent slope (°)	6	10	15
Levee	Mean height	-	10	50
	Mean (and range) of lateral angle (°)	-	13 - 21 (17)	16 - 19 (17)
Maximum block size (m)		30	6	20

Table 2 - Summary of the morphological attributes of the terrestrial analogue landslides.

The morphology, topography and texture of the Abisko landslide have three notable similarities to the CCh and ChrC landslides:

1. The erosion scar is sharp and well defined (*Fig.8c*), with the steepest values near the scar (85° in Abisko, compared to 70° in ChrC, *Fig.5b* and 52° for the CCh landslide, *Fig.5a, Table 1 & 2*) and rapidly descending to ~39° on the talus slope below.
2. The length/width ratio of the erosion zones are similar, 0.4 for the ChrC landslide, and 0.7 for the Abisko rockslide. However, in the CCh landslide the length/width ratio is 0.9. In Abisko there is no slope inversion at the end of the erosion zone as there is in ChrC and CCh (*Figs.5a & b*). Yet, the slope does lower almost to zero where the deposited material has stalled on the lower slope.

3. The deposit areas for the Abisko rockslide, and ChrC and CCh landslides are covered by blocks of tens of metres in diameter. These blocks are highlighted in *Figures 8b* by the white arrows and reach 30 m in diameter. These blocks were also noted by Rapp (1960). The deposit zone is located only on gently inclined topography in all three cases.

The two main differences between the Abisko rockslide and the ChrC and CCh landslides are their scale and a difference in the pre-existing topography. Rapp (1960) estimated that the Abisko landslide has a volume between 1×10^6 to 2×10^6 m^3, and we have calculated its volume to be 3.5×10^6 m^3 which is less than the volume of CCh and ChrC (*Table 1*). At Abisko, the adjacent hillslope has a slope of 27° (*Table 2* and *Fig.8c*), compared to 25° and 23° on Mars, for CCh and ChrC. There is a lack of a transport zone and its associated levees in the Abisko rockslide. The planview shape and mass distribution of the Abisko rockslide is more irregular than the ChrC and CCh landslides. Also, Abisko deposits is located on a non-zero surface slope, unlike the martian landslides.

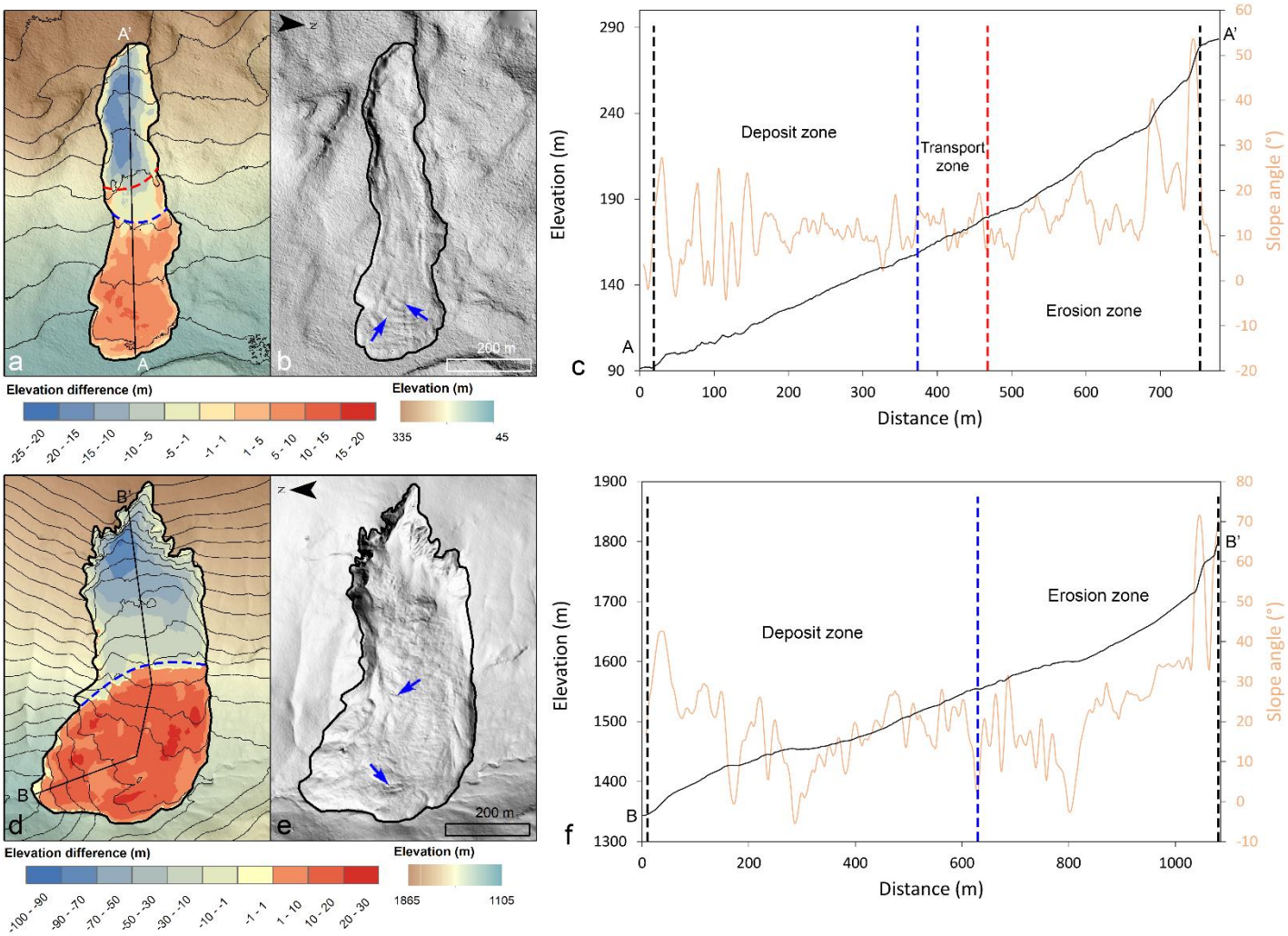

Figure 9 - Hólmavík mudslide (Iceland) and Mount Rainier mudslide (US). (a) Elevation difference map overlain on colourised DEM with semi-transparent hillshaded relief for the Hólmavík mudslide. Topographic contours with 25 m interval are marked in black. (b) Hillshaded relief of the Hólmavík mudslide. (c) Elevation profile and slope angle variation of the Hólmavík mudslide from A to A' in panel a. (d) Elevation difference map overlain on colourised DEM with semi-transparent hill-shaded relief derived from LiDAR topography for the Mount Rainier mudslide. Topographic contours with 25 m interval are marked in black. (e) Hillshaded relief image derived from LiDAR topography for the Mount Rainier mudslide. (f) Elevation profile and slope angle variation of the Mount Rainier mudslide from B to B' in panel (d). Blue arrows on panel (b) and (e) indicate ridges on the landslide deposit and dashed lines in black, red and blue indicate the erosion, transport and deposit zones. Credit: Land Survey of Iceland and Washington Lidar Portal.

Nilosyrtis Mensae analogue. The morphological analysis of NM landslide shows several similarities with terrestrial mudslides. Two terrestrial analogues have been identified, one in Iceland, near the town of Hólmavík in Iceland (65°42' N, 21°42' W, *Fig.9b*) and one in the US, near Mount Rainier in Washington State (46°59'N, 121°40'W, *Fig.9e*).

Both terrestrial examples are smaller in scale than the NM landslide but similar in shape. The similarities can be summarised as follows:

1. In both the terrestrial mudslides and in the NM landslide, the erosion scar is sharp and has an irregular outline (*Fig.9b, 9e*). The erosion zone for Hólmavík and NM has an elongate shape. The length/width ratio of the erosion zone for Hólmavík is 2.2 and for NM landslide it is 2.9 and 3.4 for northern and southern parts, respectively. For comparison the Mt Rainier mudslide has an aspect ratio of 1.5.
2. The terrestrial mudslides and the NM landslide all form along a continuous hillslope, rather than at an escarpment like the rockslides described above (*Fig.9c, 9f, Table 1 & 2*). None of these landslides has evidence for the involvement of substantial consolidated bedrock, but rather soil materials.
3. The terrestrial mudslides and the NM landslide have ridges perpendicular to the flow direction. These ridges are particularly well developed in the Hólmavík mudslide and are weakly present in the Mt Rainer mudslide. In Hólmavík they have a height of 11 m (*Fig.9b, blue arrow*) and in Mt Rainier a height of 5 m (*Fig.9e, blue arrow*), compared to 3 m on the NM landslide (*Fig.7c, blue arrow*). These compression ridges have already been observed in earthflows (Parise, 2003) and submarine landslides (Hildenbrand et al., 2006; Masson et al., 2002). Neither the terrestrial mudslides nor the NM landslide have abundant blocks at their surface.
4. Lobate margins. The terrestrial mudslides and the NM landslide all have multi-lobed terminal margins to their deposits. The relief of the margins is 12 m at Hólmavík and more than 33 m at Mt Rainier, compared to 34 m at NM (*Table 1, 2*).
5. Lateral levees. The terrestrial mudslides and the NM landslide possess lateral levees found in the transport zones of the landslides. The levees lateral slopes are 13° – 21° (*Table 2*) compared to 22° – 30° on Mars.

There are some differences between the terrestrial and martian landslide, most notably their respective sizes (*Tables 1 and 2*). A transport zone can be identified in the Hólmavík landslide, but not in the Mt Rainier and martian landslides. The terrestrial analogues also have erosion zones that are steeper than in the NM landslide and they also have a smaller underlying slope of 5 to 10° in the deposit zone compared to the martian landslide at 20° (*Tables 1 and 2*).

3.2. Age estimations of martian landslides

For the CCh landslide, we identified 12 impact craters on the deposit, and the largest of these craters has a diameter of 35 m. We used the crater-size frequency distribution of this landslide to estimate its age to be 13±5 Ma (*Fig.10a*). To obtain this estimate, we used only the 7 largest impact craters with a minimum diameter of 21 m to avoid sampling bias due to image resolution at smaller size.

For the ChrC and NM landslides, the number of craters is too low to provide an absolute age with one 23 m crater for ChrC and no craters for NM. Only an estimate of the maximum age of formation of these landslides was possible. In the case of NM, due to the lack of any impact crater, we estimated a maximum age by artificially adding the smallest diameter impact crater that we deemed to be possible

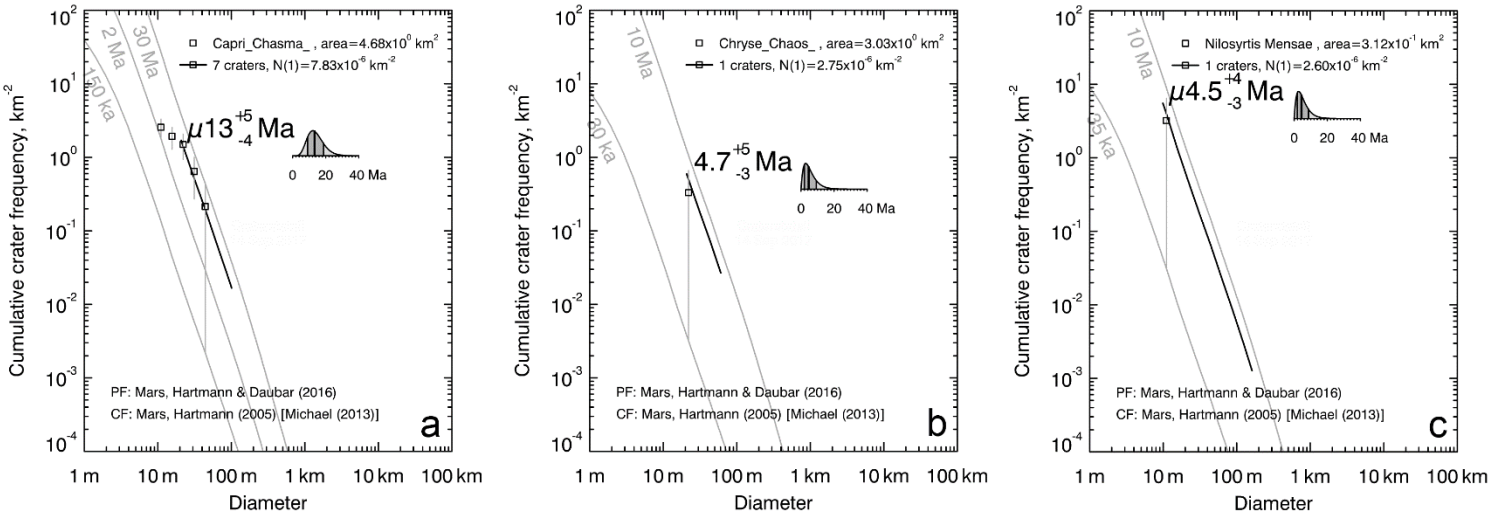

Figure 10 - Crater size-frequency plots with selected isochrons for the three dated martian landslides. (a) Capri Chasma landslide; (b) Chryse Chaos landslide; (c) Nilosyrtis Mensae landslide. PF and CF indicate the production function and chronology function, respectively. To the right of each age estimate the uncertainty is shown as a probability density function using Poisson statistics (Michael et al., 2016).

to identify in the images (10 m), a method suggested by (Hartmann, 2005). The estimated maximum age of formation of ChrC is ~4.5±4 Ma (*Fig.10b*), whereas for the NM landslide the maximum age is ~4.7±4 Ma (*Fig.10c*).

The ages obtained using this dating method do not exceed 20 Ma, hence these landslides formed recently, during the Late Amazonian.

3.3. Numerical modelling results

A summary of the friction coefficients used in the simulations along with the best-fit results are presented in Table 3. We used *L*= 5 m as the mean grain size for CCh and ChrC and *L*= 1cm for NM, based on the observed maximum block size (*see section 3.1.1*) and chosen after some sensitivity tests (*see supplementary material, S3- Grain size sensitivity tests*).

On *Figures 11*, *12* and *13* we present the simulated dynamics of the three landslides and show the deposits from our best-fit simulations alongside the observed deposits. For CCh and ChrC landsides, none of our simulations produced entirely satisfactory results. The best-fit simulation was obtained using the Pouliquen and Forterre law (*Fig.11f and 12f*) using friction angle of $\delta_1 = tan^{-1}(0.16)$, $\delta_2 = tan^{-1}(0.33)$ *and* $\delta_3 = tan^{-1}(0.19)$ for CCh and $\delta_1 = tan^{-1}(0.19)$, $\delta_2 = tan^{-1}(0.36)$ *and* $\delta_3 = tan^{-1}(0.22)$ for ChrC, and produced a closer deposit shape to the observed deposit (*Fig.11g and 12*g) than the best-fit Coulomb law simulations (*Fig.11e and 12e*) with friction angles of $\delta = tan^{-1}(0.27)$ for ChC and $\delta = tan^{-1}(0.30)$ for ChrC. The centre of mass of the simulated deposits is near the base of the slope (*Fig.11f and 12f, red point*) and compares well to the centre of mass of observed deposit (*Figure 11g and 12g, black point*). However, in the model results no substantial mass remains at the base of the erosion zone as is actually observed.

In addition, the simulated deposit is thicker in the centre and thinner towards the edges, whereas our observations show that the deposits tend to have a more constant thickness, leading to a steeper front scarp (See *Table 4*). For CCh the model underestimates the maximum deposit thickness (70-75 m in the model, *Fig.11f* and 112 m observed, *Fig.11g*) and in ChrC the model overestimates the maximum

Landslide	Initial mass (m^3)	Model parameters					Empirical Value $\mu_{eff}=V^{-0.0774}$
		Test run	Pouliquen and Forterre's law			Coulomb's law	
			$\tan(\delta_1)$	$\tan(\delta_2)$	$\tan(\delta_3)$	$\tan(\delta)$	
Capri Chasma	$9.7x10^7$	1	0.12	0.30	0.16	0.23	0.24
		2	0.14	0.32	0.18	0.25	
		3	0.16	0.33	0.19	0.26	
		4	0.18	0.35	0.21	0.27	
		5	0.19	0.37	0.23	0.28	
		6	0.21	0.39	0.25	0.29	
		7	0.23	0.41	0.27	0.30	
Chryse Chaos	$6.2x10^7$	1	0.16	0.33	0.19	0.27	0.24
		2	0.18	0.35	0.21	0.28	
		3	0.19	0.36	0.22	0.29	
		4	0.19	0.37	0.23	0.30	
		5	0.21	0.39	0.25	0.31	
		6	0.26	0.43	0.29	0.32	
		7	0.27	0.44	0.30	0.32	
Nilosyrtis Mensae	$4.2x10^6$	1	0.32	0.50	0.36	0.34	0.34
		2	0.34	0.52	0.38	0.35	
		3	0.35	0.53	0.39	0.36	
		4	0.36	0.54	0.40	0.37	
		5	0.37	0.55	0.41	0.38	
		6	0.38	0.56	0.42	0.39	
		7	0.40	0.58	0.44	0.40	

Table 3 - Summary of friction coefficient values tested for each of our three landslides using the Pouliquen and Forterre and Coulomb laws and the effective friction coefficient using the empirical law determined by Lucas et al. (2014) for landslides volume of more than 10^3 m^3. In red, the best fit coefficients are indicated. For Capri Chasma and Chryse Chaos a grain size of L=5m was used and for Nili Fossae, L=1cm. The initial mass is estimated from the difference between the observed topography and the reconstructed scar topography and differs from the deposit volumes stated in Table 1 because it includes the stalled mass in the erosion zone.

Landslide		Capri Chasma	Chryse Chaos	Nilosyrtis Mensae
Observed mean front deposit angle (°)		24	21	28
Mean simulation front deposit angle (°)	Coulomb's law	5	6	2
	Pouliquen and Forterre's law	3	4	3

Table 4 - Comparison between the front deposition angle measured in simulations using Coulomb's and Pouliquen and Forterre's laws and the real measured deposition angle. The mean angle was determined from three different measurements taken on the real and simulated deposition front.

deposit thickness (85 m in the model, *Fig.12f vs* ~64 m observed, *Fig.12g*). Finally, the modelled deposits spread over a wider area than the observed deposits in CCh and ChrC and no levees are observed, despite the fact that the Pouliquen and Forterre friction law is capable of producing levees under certain conditions (Mangeney et al., 2007).

For the NM landslide we observed a poor fit between the two-simulation law (Coulomb, *Fig.13e* and Pouliquen and Forterre, *Fig.13f*) and the observed deposit. We used friction angle $\delta = tan^{-1}(0.36)$ for Coulomb law and $\delta_1 = tan^{-1}(0.36)$, $\delta_2 = tan^{-1}(0.54)$ *and* $\delta_3 = tan^{-1}(0.40)$ for Pouliquen and Forterre law. We observed that for each law the simulated deposit centre of mass is close to the centre of mass of the observed deposit. A large proportion of the eroded mass remains within the erosion zone for each simulation.

After tests involving the release of the masses of both erosion zones at the same time and variation of the friction parameters, the best fit model produces a maximum deposit thickness of 15 m whereas it is actually ~32 m. The overall shape of the landslide is not well matched; the furthest downslope extent is located to the north of where it should be (along the steepest line of descent) (*Fig.13e and 13f*). Also, the model cannot reproduce the lateral levees observed on the real deposit (*Fig.13g*).

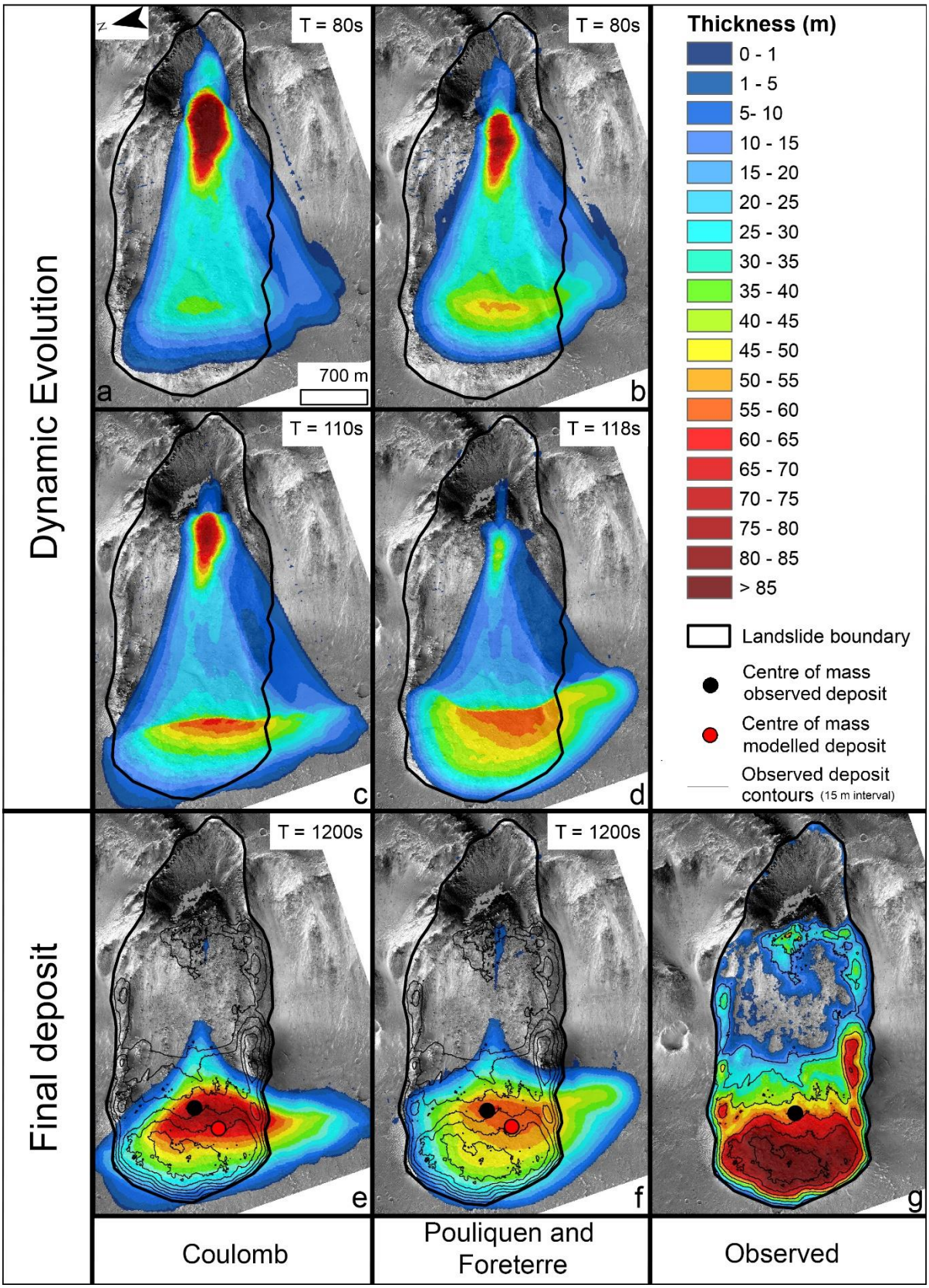

Figure 11 – Modelled and observed deposit thicknesses for Capri Chasma landslide. (a-d) Dynamic evolution of the deposits for grain size L=5m using Coulomb's law at T=80s (a), T=110s (c) and T=1200s (e) and using Pouliquen and Forterre law (2002) at T=80s (b), T=118s (d) and T=1200s (f). The times at 1200s represent fully stabilised deposits. (g) The observed deposit. The simulations focused on reproducing the final morphology of the deposits, so the timesteps during the simulation are provided here to illustrate the dynamics in the model. Background image HiRISE ESP_035831_1760. Credit: NASA/JPL/UofA.

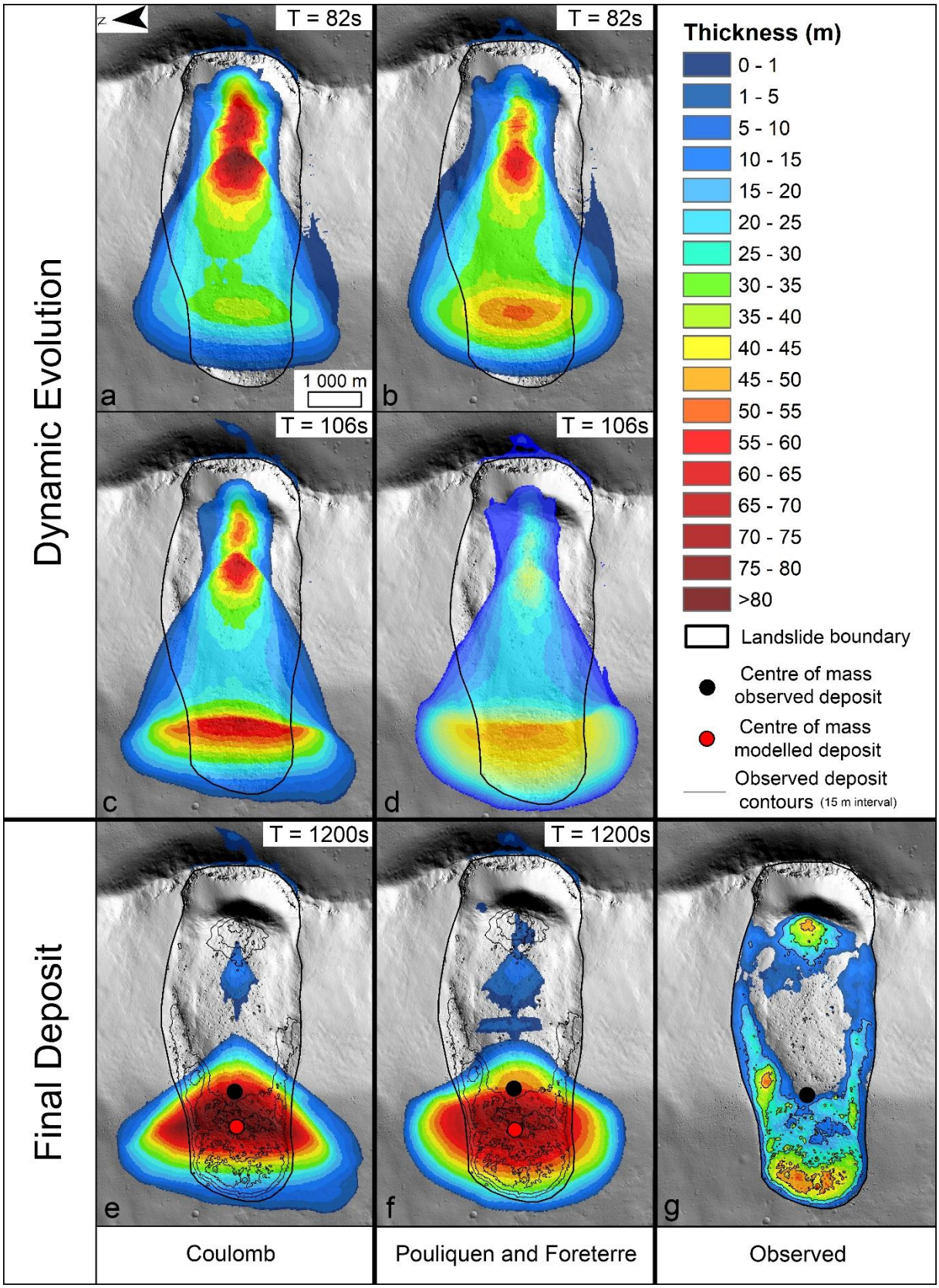

Figure 12 - Dynamic evolution of Chryse Chaos landslide modelling for grain size L=5m using Coulomb's law at T=82s (a), T=106s (c) and T=1200s (e) and using Pouliquen and Forterre law, 2002 at T=82s (b), T=106s (d) and T=1200s (f). The times at 1200s represent fully stabilised deposits. The observed deposit (g). The simulations focused on reproducing the final morphology of the deposits, so the timesteps during the simulation are provided here to illustrate the dynamics in the model. Background is the hillshaded relief rendering of the DEM.

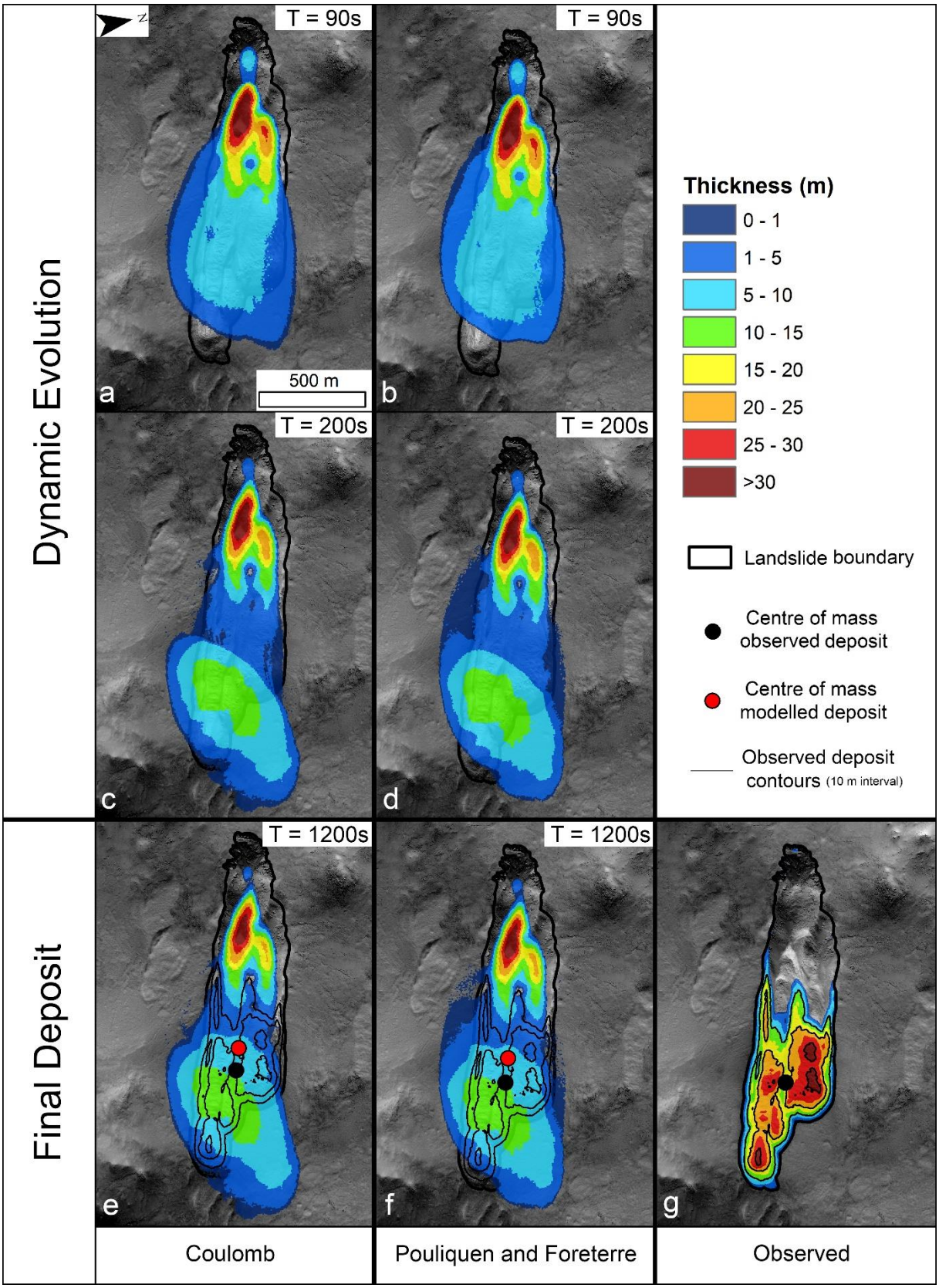

Figure 13 - Dynamic evolution of Nili Fossae landslide modelling for grain size L=1cm using Coulomb's law at T=90s (a), T=200s (c) and T=1200s (e) and using Pouliquen and Forterre law (2002) at T=90s (b), T=200s (d) and T=1200s (f). The times at 1200s represent fully stabilised deposits. The observed deposit (g). The simulations focused on reproducing the final morphology of the deposits, so the timesteps during the simulation are provided here to illustrate the dynamics in the model. Background is HiRISE image ESP_026781_2075. Image credits: NASA/JPL/UofA.

4. Discussion

In the following sections, we will first discuss how the investigated landslides compare to other martian and terrestrial landslides, and then their likely emplacement mechanisms suggested by our geomorphic observations and numerical modelling. Finally, we propose different scenarios that could have led to the formation of these landslides.

4.1. Comparison with other martian landslides

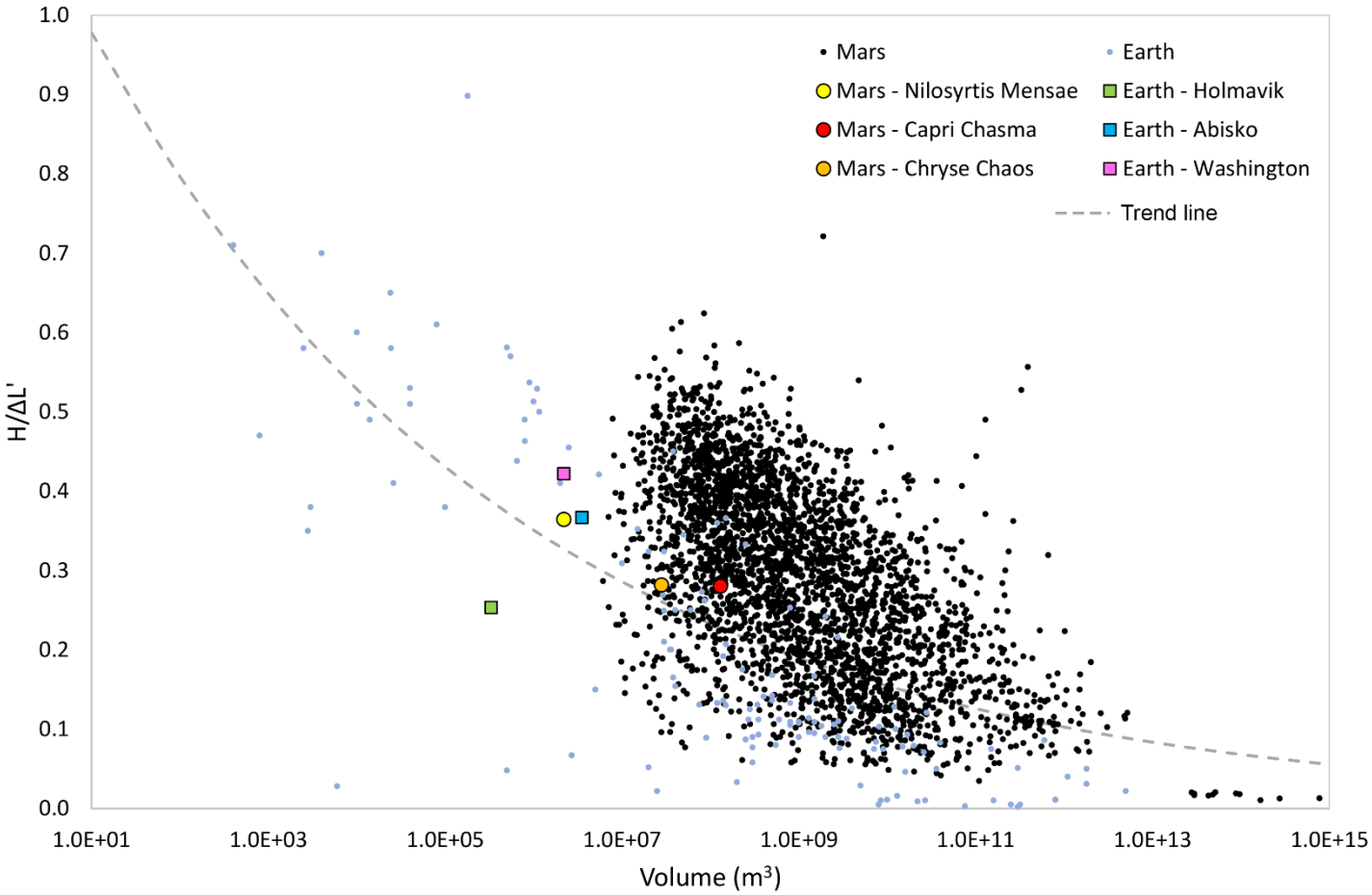

Figure 14 - Heim's ratio (H/ΔL') plotted against volume for the martian landslides (coloured dots) and terrestrial landslides (coloured squares) of this study compared to terrestrial (blue dots, data from Legros et al., 2002, Lucas et al. 2014) and martian landslides (black dots, data from Quantin et al., 2004; Brunetti et al., 2014 ; Lucas et al. 2014 ; Crosta et al., 2018).

Context. The morphology of the three martian landslides studied here differs from that found in previous studies of landslides on Mars, which mostly focused on the large landslides in Valles Marineris (Lucchitta, 1979; McEwen, 1989; Shaller, 1991; Quantin et al., 2004a; Soukhovitskaya and Manga, 2006; De Blasio, 2011; Brunetti et al., 2014; Airo, 2015). These large landslides have a very large deposition area with an average of 10^9 m² (Quantin et al., 2004a) while our landslides have deposition areas ranging from 10^5 to 10^6 m². The large landslides in Valles Marineris often have overlapping layers of deposits (Grindrod and Warner, 2014) and longitudinal furrows (De Blasio, 2011; Magnarini et al., 2019), which is not the case for the three landslides presented here. Some Valles Marineris landslides do have deposit zones with a similar width to their erosion zones (*Fig.4a, orange arrows*) as found in our landslides.

When we compare the Heim's ratio (*see section 2.1.3*) and volume of our three martian landslides with the martian and terrestrial landslides from the literature (Legros, 2002; Quantin et al., 2004a; Lucas et al., 2014; Brunetti et al., 2014; Crosta et al., 2018) we observe that CCh and ChrC are towards the smaller end of the typical volumes or martian landslides and NM falls outside the martian population (*Fig.14*). Despite a gravitational difference between the Earth and Mars, the comparison between landslides is still possible because in the case of dry landslides, the flow is governed by the balance between the driving and resistance forces that are all proportional to the surface gravity (Johnson and Campbell, 2017). More specifically, only the velocity u and stopping time t_f depend on g (Mangeney-Castelnau et al., 2005; Mangeney et al., 2010). As described in Mangeney et al. (2010), the constant acceleration resulting from the sum of forces due to gravity (c_0) and friction (m), are defined as $c_0 = \sqrt{kgh_0\,cos\,\theta}$ and $m = g\,cos\,\theta(tan\,\theta - tan\,\delta)$, with k being a constant, θ is the slope inclination and h_0 the initial thickness. The front of the landslide stops when its velocity $u = 2c_0 + mt_f = 0$, with the stopping time (t_f) defined as:

$$t_f = \frac{2\sqrt{k}}{\tan\delta - \tan\theta}\tau_c \qquad (5)$$

where $\tau_c = \sqrt{h_0/(g\cos\theta)}$, the characteristic free fall time.

In case of the Coulomb friction law where $\mu = tan\,\delta$ is constant, there is no dependency on gravity. But in case of the Pouliquen and Forterre friction law, as can be seen in *Section 2.3.3 equation (1)*, gravity is involved in the friction coefficient calculation, and in this case if g decreases, the friction coefficient increases, so the velocity decreases.

Our martian landslides are located along the trend line predicted by Lucas et al. (2014) as calculated from the landslides used in their study where $\frac{H}{\Delta L'} = 1.2 \times V^{-0.089}$ with V being the volume of the landslide. This trend line (grey dashed line, *Fig.14*) was calculated for landslides with mainly dry granular behaviour. As our landslides roughly follow this trend line, this is consistent with them having a dry granular behaviour, but does not exclude other mechanisms. This trend line does not take into account the morphology of the deposits which is another key indicator of the physical processes at work during the flow, as will be discussed below.

Age. We estimate the age of these three martian landslides to be less than 20 Ma, subject to a large margin of error given the small surface area of these landslides and the size of the craters used to perform the dating (e.g., Warner et al., 2015). The older age of CCh compared to ChrC landslide is corroborated by the lower frequency of large blocks at the surface of the deposits of ChC compared to ChrC and may be related to the breakdown of rocks over time (e.g., de Haas et al., 2013). Figure 15 further illustrates this point, showing a landslide with a high frequency of superposed craters (so presumably older than both CCh and ChrC) located near Montevallo crater (15°;54 °W) (*Fig.15a*). On this landslide the blocks are less numerous and less visible (*Fig.15b*), possibly covered by aeolian deposits, whereas a lot of blocks are still visible on the fresh landslide (*Fig.15d*). Whether or not water was involved in the formation of the ancient landslides in Valles Marineris is still under debate, because the climate could have been favourable to liquid water before the Amazonian. In the case of our studied landslides, they formed under recent martian climate conditions, which are thought to be similar to the present one, that is, dominated by cold temperatures and low atmospheric pressure, and for which the distribution of volatiles in is limited to within the ground at mid-and high-latitudes (e.g., Head et al., 2003).

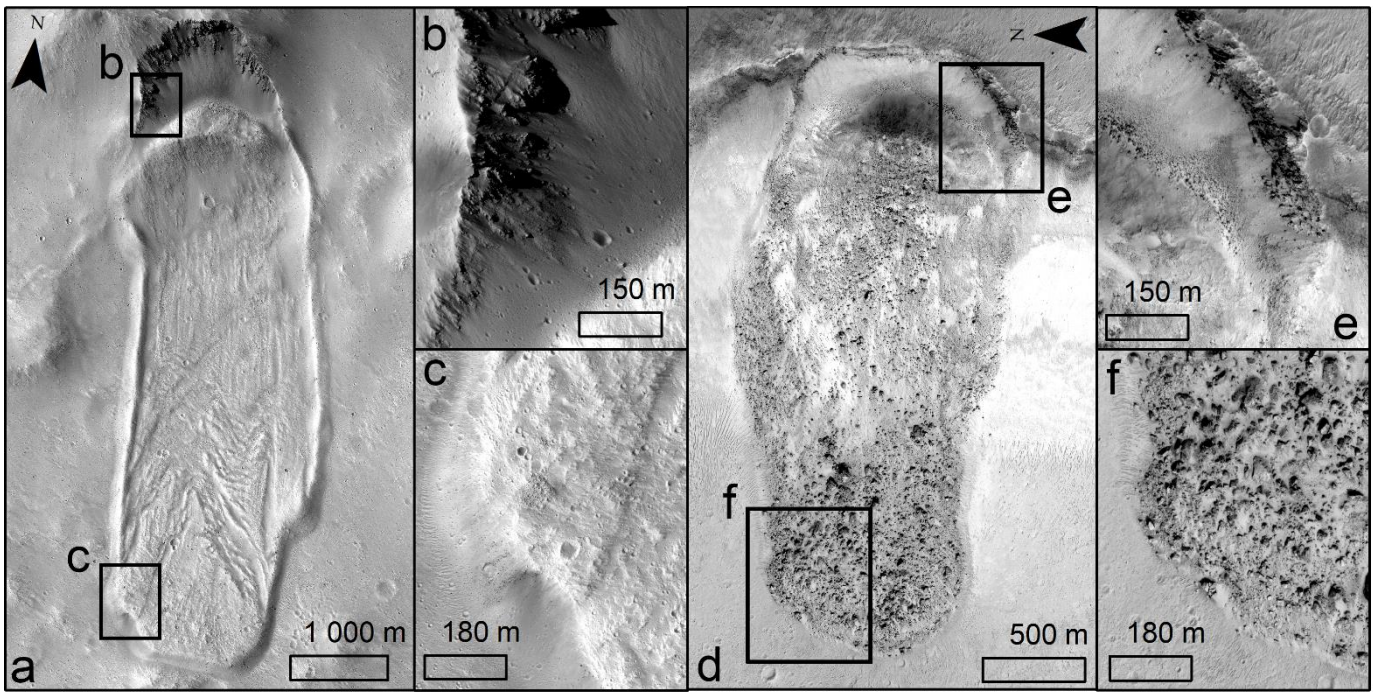

Figure 15 - Morphological comparison between a degraded landslide (a) and a fresh landslide (d). (a) Landslide in Montevallo crater (15°N; 54°W). (b) Detailed view of the erosion zone showing multiple superposed craters and few visible blocks at the foot of the talus. (c) Detailed view of the deposition zone with superposed craters and a scattering of barely resolvable blocks. (d) Capri Chasma landslide (this study). (e) Detailed view of the erosion zone showing blocks at the foot of the talus slope and tracks from rolling blocks and no visible craters. (f) Detailed view of the deposition zone with densely packed large blocks and no visible impact craters. HiRISE images a, b, c: ESP_027643_1955; d, e, f: ESP_050033_1920. Credits: NASA/JPL/UofA.

4.2. Emplacement mechanisms

4.2.1. Geomorphic constraints

Comparison between the three martian landslides. Though the landslides of CCh and ChrC are similar, two main features set them apart. Firstly, for the ChrC landslide, we observed a raised rim present upslope of the erosion zone, just above the scar (*Fig.16a white arrows and Fig.16c & d, black arrows*), which is not present in the CCh landslide. We suggest that this raised topography could be the remnants of a rim of an impact crater, which formed before the Chryse outflow channel and therefore could be a location of pre-existing weakness. Secondly, the overall morphology of the CCh landslide appears more degraded, which is consistent with its older age from the crater size-frequency distribution analysis (Section 3.2). It has fewer and smaller (40 m compared to 60 m for ChrC, *Table 1*) visible blocks at the surface. The blocks in the deposition area of CCh may have been covered by windblown deposits, or broken down (de Haas et al., 2013). The surface roughness is lower for CCh than for the ChrC landslide. The older age of the CCh landslide could also explain why the slopes in the erosion zone are lower than in the ChrC landslide (30° compared to 35°, *Table 1*). Despite these differences, the similarities in topographic setting and morphological features (levees, deposit thickness, blocky surface texture) indicate these landslides had a very similar formation mechanism.

In contrast, the NM landslide has morphological characteristics that allow it to be easily distinguished from the other two landslides studied. The first difference lies in the shape of the erosion zones. In the case of CCh and ChrC landslide, the landslide scar forms a well-marked single arc, while for NM the scar is irregular. The slope profiles of the landslides shown in *Figure 5* show the similarity between the landslides of CCh and ChrC, where the scar is located at a sudden change in the slope of the

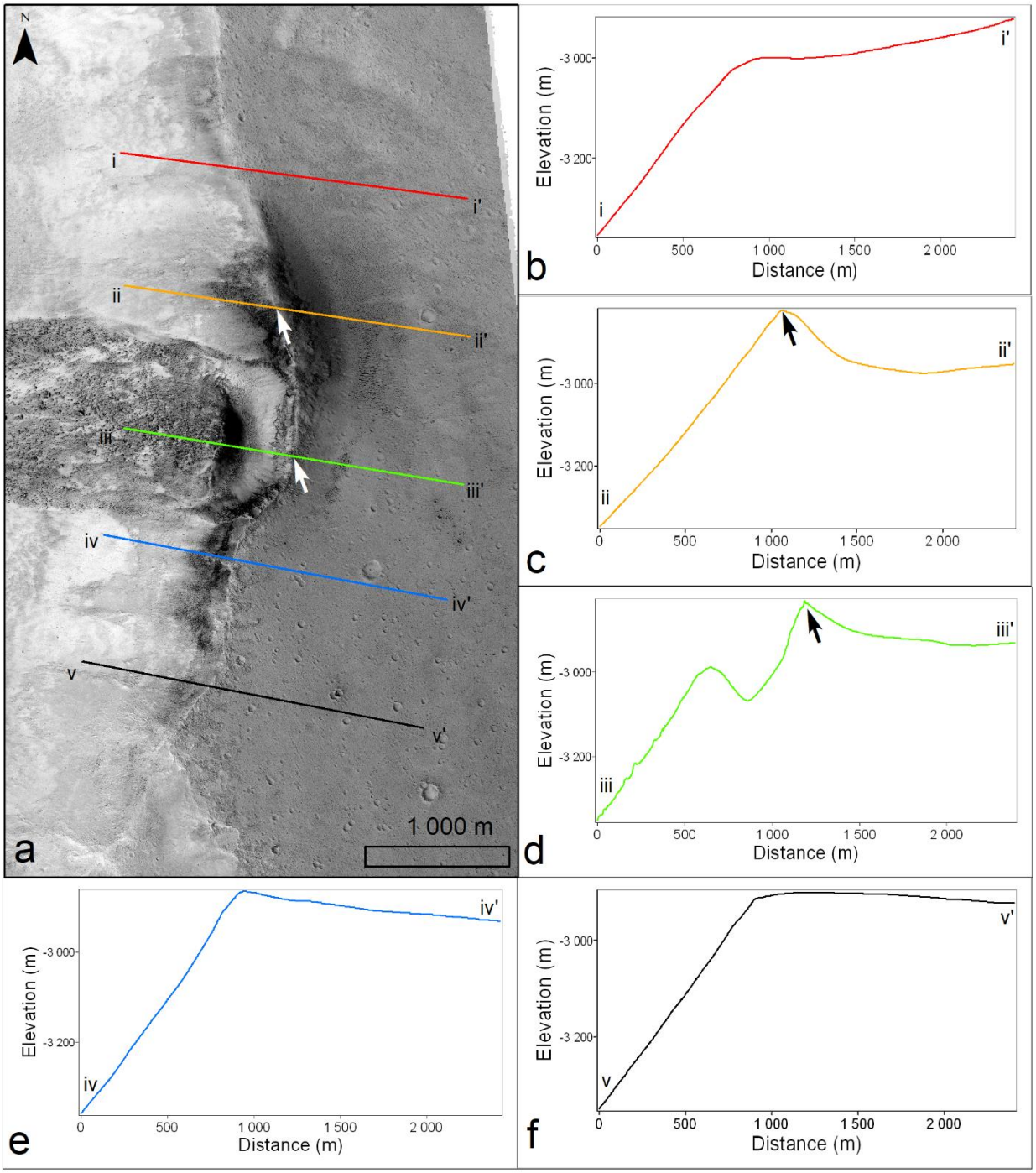

Figure 16 - (a) HiRISE image PSP_005701_1920 of Chryse Chaos landslide where the position of the profiles in panels b-f are indicated in corresponding colours. (b) to (f) Show a series of topographic profiles across the escarpment of the Chryse Chaos mesa progressing from north to south. Black arrows on profiles c and d correspond to white arrows on the HiRISE image in a and highlight the possible raised rim of a remnant impact crater. Credit: NASA/JPL/UofA.

topography. Furthermore, the erosion zone contains a slope inversion at its base where materials have stalled. On the contrary, the NM landslide scar is located in the middle of a continuous 25° slope, and no slope inversion is visible at the base of the erosion zone. The images and the oscillations in the slope profiles (*Fig. 5*) show that the deposit zones of CCh and ChrC are dominated by large blocks, whereas the NM landslide has a lower size and density of blocks on the deposit surface. These blocks seem to have been re-entrained from the middle lobe by the movement of the southern lobe (*Fig.7c, white arrow*). We infer that the final morphology of the NM deposits results from at least two events. In the

NM landslide, there are ridges perpendicular to the direction of flow in the deposition zone, which are not found on the CCh and ChrC landslides. Finally, the deposition front of the NM landslide has a multi-lobe shape that is not found in the CCh and ChrC landslides, which have a gently curved flow front. The levees are also less marked on the CCh and ChrC landslides than on the NM landslide.

The morphological differences indicate different flow dynamics between the CCh/ChrC landslides and the NM landslide.

Comparison between martian landslides and terrestrial analogues. Here, we use our comparison to terrestrial analogues presented in Section 3.1.2 to infer formation mechanisms for the martian landslides. For CCh and ChrC, the rockslide near Abisko has similar topographic and morphological features, including: the erosion scar, which is well defined, the erosion zone with similar slopes angle and a deposition zone with blocks of 30 m in diameter distributed over the entire surface. However, we also noted some morphological differences, which we argue can be explained by the shape and size of the pre-existing slope rather than differing formation mechanisms. At Abisko, the hillslope has a height and slope of 170 m and 27° (*Table 2*, *Fig.8c*), compared to ~1000 m and 25° on Mars (*Table 1*, *Fig.5*). This difference results in a lack of a transport zone and therefore can explain the lack of levees in the Abisko rockslide, as the erosion and deposit zones are directly adjacent. Where there is an extended transport zone, other rockslides do show low-slope external levees (e.g., Shea and van Wyk de Vries, 2008). The planview shape and mass distribution of the Abisko rockslide is more irregular and the deposits have a non-zero surface slope, unlike the ChrC and CCh landslides. We attribute these features to the difference in the topography underlying the deposit zone: the valley floor is not flat in Abikso (6°) and is irregular unlike on Mars (slope < 3° and relatively smooth). Hence, we conclude that the similarities observed between the Abisko and ChrC and CCh landslides imply similar formation mechanism - catastrophic bedrock failure, whose downslope transport was driven by the action of gravity. McSaveney and Davies (2007) describe the mechanism behind rockslides, as a simple gravity driven movement of bedrock downslope. They usually have a single erosion surface, or thin zones of intense shear strain (McSaveney and Davies, 2007).

As described in Section 3.1.2 we observed several key similarities between the NM landslide and the mudslides of Mt. Rainer and Hólmavík: i) the scar and the erosion zone share the same irregular characteristics, ii) the landslides occur on a continuous low slope and iii) in the deposit zone there are levees, ridges perpendicular to the direction of the flow, few large blocks and a multi-lobate front. The difference in thickness between the martian landslide and the terrestrial landslides can be accounted for by the difference in volume between the landslides (Tables 1 and 2).

The presence of lateral levees on its own is not diagnostic. Lateral levees in landslides can be produced by a variety of different mechanisms, as detailed by Corominas (1994). Indeed, the flow can cause basal erosion, which results in lowering of the centre of the sliding mass, leaving lateral levees on either side of the landslide. On Earth, lateral levees are a common signature of earthflows and debris flows (Baum et al., 2014; Nereson and Finnegan, 2015). Earthflows are mainly composed of clays and contain water which plays an important role in the landslide's mobility (Baum et al., 2014). Levees can also be produced in dry granular landslides so do not necessarily indicate the presence of clay and/or water as shown by Mangeney et al. (2007) and Félix and Thomas (2004). Here we observe lateral levees with exterior slopes of ~25°, quite similar to those observed on pyroclastic flow deposits in Chile, between 20° and 25° (e.g., *Figure 9* of Jessop et al., 2012) whereas granular materials in laboratory tend to have lower slopes (e.g., Félix and Thomas, 2004). The higher levee angle observed for these pyroclastic flows

has been suggested to be linked to the high polydispersity of the material involved. For the NM landslide, it could be the presence of clays or polydisperse granular materials that cause these high-standing steep levees, but given the other morphological similarities to mudslides we favour the presence of clays.

The morphology of mudslides on Earth is controlled by the viscous deformation of the substrate, which is in turn controlled by the degree of water saturation of the interstitial environment and the substrate mechanical properties (Comegna et al., 2007). To form a mudslide, clay size grains and liquid water are needed (Vallf-Jo, 1979) and involve variable proportions of water and clay minerals in the case of earthflows. This raises the question of the importance of clays in the formation of the NM landslide.

Near infrared orbital spectra of the landslide region show the presence of clay minerals likely formed by hydrothermal activity (Mangold et al., 2007; Ehlmann et al., 2009; Michalski et al., 2010; Viviano et al., 2013), although locations have showed possible weathering through pedogenetic alteration as well (Gaudin et al., 2011). Clay minerals corresponding to Fe/Mg-phyllosilicates are observed on the bedrock of the impact crater rim where the NM landslide occurs (see supplementary material, *S1-Spectral analysis*, *Figure.S1*). However, the landslide deposit itself does not exhibit any clear spectral signature of clays and it seems to be associated with a light-toned unit mantling this clay-rich bedrock rather than to the bedrock itself. Thus, even if the occurrence of clay minerals in the landslide deposit should favour mudslide development, no clear relationship can be demonstrated between the clay-rich bedrock and the material mobilised by the landslide. As mudslides on Earth necessarily involve liquid water, the morphological similarities with the NM landslide suggest liquid water might also be involved at this location. However, the dating of this landslide to the late Amazonian means it occurred during a period when liquid water is expected to be rare at the surface of Mars, as discussed further below.

Given the morphological comparison between the landslides of CCh, ChrC and NM and their respective terrestrial analogues, we classify them into two distinct categories. CCh and ChrC are found to be most similar to landslides that fall into the rockslide category and NM in the mudslide category. We used these morphological constraints to inform the numerical modelling of the CCh/ChrC and NM landslides.

4.2.2. Numerical modelling

Capri Chasma/Chryse Chaos simulations. The difference observed between our simulation and the observed deposit (i.e., the final shape of the deposit) could be partly due to the shape of the reconstructed erosion zone that, being partly covered by deposits, was hard to constrain accurately. Tests using a flatter base within the erosion zone do lead to more deposited mass in this zone, as illustrated in the Supplementary material (*section S4- Topographic reconstructions*), but not as much as is observed.

The lack of deposits in the erosion zone and on the sloping terrain where the levees are deposited suggests that the best-fit friction coefficient models a landslide that is too mobile (a lower friction coefficient than the one considered in the simulations).

The absence of levees means that the deposits spread out more than observed and that the conditions for the formation of such levees have not been satisfied. These differences between the model and the observed deposits do not invalidate the granular flow (rockslide) hypothesis, but highlight that this

model makes assumptions which prevent some important complexities being considered. As this model has been successfully used for larger landslides in Valles Marineris, it is likely that these complexities become dominant at smaller scales. For example, at smaller spatial scales the timescale of the mass release becomes more important with respect to the timescale of the sliding.

In SHALTOP the eroded mass is released instantaneously, but levees are observed in experiments only when supply is continuous and not from instantaneous collapse experiments (e.g., Félix and Thomas, 2004). Besides, the height of the levees simulated with the Pouliquen and Forterre's law has been shown to be too small compared to granular flow experiments (Mangeney et al., 2007; Rocha et al., 2019). This type of landslide seems to follow a sliding plane, so a multi-layer model may be more appropriate as it is able to simulate the heterogeneity in the vertical direction (Fernandez-Nieto et al., 2016).

Comparison of our results with laboratory experiments on granular flows (Pouliquen and Forterre, 2002) suggest that the dynamics could be quite different if the presence of an erodible bed were included in the simulations, in this case the internal deformation may play a less important role. Pouliquen and Forterre (2002) noted the difference between the spreading of a granular cap over a rigid bed (*Figure 5a* of Pouliquen and Forterre, 2002) and over an erodible bed. With an erodible bed, there was a steeper front and the flowing mass had a more 'croissant' shape (Pouliquen and Forterre, 2002, see also Mangeney et al., 2007), which are attributes expressed by our observed deposits. The development of a steeper front in the presence of an erodible bed is also observed for simulations at the field scale (Moretti et al., 2012) (their *Figures 2c* and *2f*). The erodible bed on Mars could be provided by the talus slope over which the landslides propagate.

Nilosyrtis Mensae simulation. Despite the fitting of the centre of mass and runout, the model provides a poor fit for the observed morphology for both of the applied friction laws. We observed that a large proportion of mass remains in the erosion zone for both simulations that is not observed on the real deposit. These observations suggest that NM landslide is less mobile than the model predicts.

The failure of the model to reproduce the morphology does not necessarily invalidate the granular flow mechanism for this landslide, but the aspects where the model fails suggests that this landslide is not behaving like a granular flow. Firstly, the fact that the deposits do not follow the steepest line of descent suggests they are momentum dominated. Second, the mass being released from a low-slope fracture zone suggest, given its morphology, some cohesion within the deposits, which is not predicted by the granular flow model.

In general, the dry granular flow laws in SHALTOP cannot reproduce satisfactorily any of these martian landslides, but produces a closer fit for the landslides interpreted as rockslides. We suggest that possible improvements to the model, such as: gradual release of the mass, inclusion of an erodible bed and/or adjusting the law used to model the rheology of the landslide may result in better fits and could be the object of future work.

4.3. Formation scenario

On Earth, landslides can be triggered by various phenomena, such as earthquakes (Meunier et al., 2007), heavy rainfall (Wang et al., 2002) or melting permafrost (Niu et al., 2015). We will not consider liquid water as a factor in the landslides of CCh and ChrC, as their morphology is not compatible with its involvement. We therefore discuss the possible role that seismic shaking could have had in

triggering these recent landslides. For the NM landslide, we will consider among other things the potential roles of liquid water and seismic shaking as triggering factor(s).

4.3.1. The recent formation of Capri Chasma and Chryse Chaos landslides

On Earth, seismic activity can cause landslides (e.g., Strecker and Fauque, 1988; Bommer and Rodríguez, 2002; Chen et al., 2006; Chigira et al., 2010; Sepúlveda et al., 2010). Earthquakes can destabilize the hydrogeological environment and after repeated earthquakes can cause landslides (e.g., Sassa et al., 2007; Walter and Joswig, 2008; Sæmundsson et al., 2018). A seismic origin has also been considered for martian landslides (e.g., Schultz, 2002; Quantin et al., 2004b). The source of the seismic activity could be tectonic: evidence for recent crustal seismicity in the zone of our landslides comes in the form of faults cutting through the large landslides in Valles Marineris, which are <1 Ga (Quantin et al., 2004a), and wrinkle ridges and/or blind faults (e.g., Schultz, 2000) which are found within 30 km of the CCh and ChrC landslides. In addition, recent results from the InSight instrument Seismic Experiment for Interior Structure (SEIS, (Lognonné et al., 2019) provide evidence for marsquakes, probably related to upper crustal structures (Giardini et al., 2020).

Alternatively, seismic shaking could be caused by meteorite impacts. Teanby and Wookey (2011) estimate that an earthquake with a magnitude between 3.9 and 4.5 could be generated by a meteorite impact forming a crater with a diameter between 617 and 1280 m. The SEIS instrument on the InSight lander has not yet been able to link seismic detection with certainty to a meteorite impact, but a study by Wójcicka et al. (2020) estimates that the instrument would be capable of detecting an impact of more than 10 m in diameter within a radius of 400 km. At least five impact craters with a diameter up to 617 m and with preserved ejecta (indicating a young age) have been identified around the landslides but it is currently not possible to directly link the formation of these impact craters to the formation of one of our landslides.

Given the evidence, we conclude that seismic shaking from a nearby meteorite impact, or from a crustal marsquake are equally likely triggers for these landslides.

4.3.2. The recent formation of Nilosyrtis Mensae landslide

We have identified morphological similarities between the NM landslide and terrestrial mudslides, including the lobate margins, lateral levees and ridges perpendicular to the flow direction. On Earth, mudslides are caused by water saturation of the surface materials. Saturation causes a loss of cohesion by increasing pore pressure and increases the weight of the materials, allowing them to flow on relatively low slopes (e.g., Chandler, 1972). Saturation can occur throughout, causing deformation *en masse* of the material, or can occur in a particular layer, causing the material above it to slide (e.g., Comegna et al., 2007). On Mars, the NM landslide is dated to a maximum of ~4.7±4 Ma and thus formed near the end of the Late Amazonian period (3.1 Ga to present). It is generally accepted that this period is dominated by hyper-arid conditions hostile to the existence of surface liquid water (e.g., Baker et al., 1991; Ehlmann et al., 2011). The question is therefore: how could water have contributed to the formation of the landslide? As above, we first examine the potential role of seismicity, which can play a role in bringing water to the surface. We then discuss climatic factors and geothermal heat flow.

Seismic activity. On Earth, earthquakes can trigger mudslides via two main mechanisms: liquefaction and aquifer perturbation with saturation of unstable formations (e.g., Binet et al., 2007; Marc et al.,

2015). For the NM landslide, we searched for evidence of recent tectonic activity or meteorite impacts that may have triggered the landslide. The Nili Fossae region is known for its extensive fault system, but we found no convincing evidence for recent faults or recent activity near the host crater. We found three young impact craters (ranging in diameter from 2,500 to 3,700 m) but all appear to be somewhat degraded. It therefore seems unlikely that seismic activity played a role in forming the landslide.

Influence of climate. The latitude of the NM landslide is just beyond the generally recognised limit of 30° for discontinuous ground ice (e.g., Mustard et al., 2001), but considering Mars' frequent changes in obliquity we consider it likely that ice could have been present in the ground at the time of the landslide. Indeed, Mars is thought to have undergone a significant downward shift in average obliquity at ~5 Ma (Laskar et al., 2004), which roughly corresponds to our estimated maximum age of the NM landslide at 4.7±4 Ma. This shift destabilised ice deposits at the mid-latitudes causing them to migrate back towards the poles (Laskar et al., 2004). It has been hypothesised that the thermal disequilibrium caused by such obliquity shifts could melt ground ice in the first metre of the subsurface (Costard et al., 2002), but that melting over a thickness >10 m is extremely unlikely (e.g., Kreslavsky et al., 2008; Mellon and Phillips, 2001). Hence, this mechanism seems inadequate to trigger a landslide, whose erosion zone penetrates to 50 m below the surface (*Fig.5c*).

Water and ice interaction. The impact crater where NM landslide occurs also contain three other landslides with a same morphology which may have a similar formation mechanism. As discussed above, we consider that ice could have been present in the ground when the landslides formed. We then need an external mechanism to melt this ice. Recent work has revealed that basal melting of debris-covered glaciers may be triggered by a locally higher geothermal flow (Gallagher and Balme, 2015; Butcher et al., 2017). Clay minerals formed by hydrothermal activity have been previously identify in the Nili Fossae region (Ehlmann et al., 2009; Brown et al., 2010; Viviano et al., 2013). They reveal the presence of geothermal heat flow in the region mostly active during the early to middle Noachian (Ehlmann et al., 2011). The presence of remnant and localised geothermal flux in this impact crater could explain why this type of landslide is not observed elsewhere in the region but this hypothesis needs to be qualified by the fact that the crater itself is at least 3 billion years old and itself is unlikely to represent the source of the recent active heating. Nevertheless, the crater wall is a preferential location for fluids, due to the presence of fractures potentially linking to surface deep aquifers under pressure (e.g., Abotalib and Heggy, 2019).

In summary, no option is fully satisfying, but we consider that triggering by ground ice melt, via increased geothermal heat flux, is an attractive hypothesis to further develop in future work.

5. Conclusions

We have studied three martian landslides using high-resolution images and digital elevation models, comparison with Earth analogues and numerical simulations. The aim is to deduce hypotheses of landslide formation on Mars where in situ analysis is generally not possible. Our results show the importance of using morphological comparison between martian and terrestrial landslides to identify key morphologies, combined with numerical modelling.

We estimate that these landslides are all very recent, possibly formed less than 20 Ma and their morphological attributes suggest two distinct behaviours. The Capri Chasma and Chryse Chaos landslides are both located in equatorial regions and share similarities in shape and morphometric

characteristics with rockslides on Earth. We consider it likely that these landslides were a result of bedrock failure induced by seismic shaking brought about by nearby impacts or crustal Marsquakes.

In contrast, the morphology of the Nilosyrtis Mensae landslide is different from the CCh and ChrC landslides and is more similar to terrestrial mudslides. Similarities include the presence of levees, lobate fronts and ridges perpendicular to the direction of sliding. This suggests a role of clay-sized grains, perhaps related to the presence of phyllosilicates in this region, and of recent, local episodes of liquid water release. We hypothesise that this landslide could have been caused by melting of ground ice by locally elevated geothermal heat flux, and further investigations are currently underway in the Nilosyrtis Mensae area to support or refute this hypothesis.

Acknowledgments

We are grateful to G. Stucky de Quay and another anonymous reviewer for improving the quality of the manuscript with their helpful feedback. S .J. Conway, N. Mangold and A. Guimpier are grateful for the support of the Programme National de Planétologie (PNP), the Centre National d'Etudes Spatiales (CNES), the Groupement de Recherche Ecoulements Gravitaires et RIsques Naturels (EGRIN) and A. Mangeney for the ERC contract , ERC-CG-2013-PE10-617472 SLIDEQUAKES**.** M. Pajola, A. Lucchetti and G. Munaretto have been supported for this study by the Italian Space Agency (ASI-INAF agreement no. 2017-03-17). The authors thank the spacecraft and instrument engineering teams for the successful completion and operation of CaSSIS. CaSSIS is a project of the University of Bern funded through the Swiss Space Office via ESA's PRODEX programme. The instrument hardware development was also supported by the Italian Space Agency (ASI) (ASI-INAF agreement no. I/018/12/0), INAF/ Astronomical Observatory of Padova, and the Space Research Center (CBK) in Warsaw. Support from SGF (Budapest), the University of Arizona (LPL) and NASA are also gratefully acknowledged.

References

Abotalib, A.Z., Heggy, E., 2019. A deep groundwater origin for recurring slope lineae on Mars. Nat. Geosci. 12, 235–241. https://doi.org/10.1038/s41561-019-0327-5

Airo, A., 2015. Landslide (Mars), in: Gargaud, M., Irvine, W.M., Amils, R., Cleaves, H.J. (Jim), Pinti, D.L., Quintanilla, J.C., Rouan, D., Spohn, T., Tirard, S., Viso, M. (Eds.), Encyclopedia of Astrobiology. Springer Berlin Heidelberg, Berlin, Heidelberg, pp. 1358–1359. https://doi.org/10.1007/978-3-662-44185-5_2473

Baker, V.R., Strom, R.G., Gulick, V.C., Kargel, J.S., Komatsu, G., Kale, V.S., 1991. Ancient oceans, ice sheets and the hydrological cycle on Mars. Nature 352, 589–594. https://doi.org/10.1038/352589a0

Baum, R.L., Savage, W.Z., Wasowski, J., 2014. Mechanics of earth flows 9.

Bibring, J.-P., Langevin, Y., Gendrin, A., Gondet, B., Poulet, F., Berthé, M., Soufflot, A., Arvidson, R., Mangold, N., Mustard, J., Drossart, P., Team OMEGA, 2005. Mars Surface Diversity as Revealed by the OMEGA/Mars Express Observations. Science 307, 1576–1581. https://doi.org/10.1126/science.1108806

Binet, S., Mudry, J., Scavia, C., Campus, S., Bertrand, C., Guglielmi, Y., 2007. In situ characterization of flows in a fractured unstable slope. Geomorphology 86, 193–203. https://doi.org/10.1016/j.geomorph.2006.08.013

Blair, T.C., McPherson, J.G., 1999. Grain-size and textural classification of coarse sedimentary particles. J. Sediment. Res. 69, 6–19. https://doi.org/10.2110/jsr.69.6

Bommer, J.J., Rodríguez, C.E., 2002. Earthquake-induced landslides in Central America. Eng. Geol. 63, 189–220. https://doi.org/10.1016/S0013-7952(01)00081-3

Bouchut, F., Mangeney-Castelnau, A., Perthame, B., Vilotte, J.-P., 2003. A new model of Saint Venant and Savage–Hutter type for gravity driven shallow water flows. Comptes Rendus Math. 336, 531–536. https://doi.org/10.1016/S1631-073X(03)00117-1

Bouchut, F., Westdickenberg, M., 2004. Gravity driven shallow water models for arbitrary topography. Commun. Math. Sci. 2, 359–389.

Brown, A.J., Hook, S.J., Baldridge, A.M., Crowley, J.K., Bridges, N.T., Thomson, B.J., Marion, G.M., de Souza Filho, C.R., Bishop, J.L., 2010. Hydrothermal formation of Clay-Carbonate alteration assemblages in the Nili Fossae region of Mars. Earth Planet. Sci. Lett. 297, 174–182. https://doi.org/10.1016/j.epsl.2010.06.018

Brunet, M., Moretti, L., Le Friant, A., Mangeney, A., Fernández Nieto, E.D., Bouchut, F., 2017. Numerical simulation of the 30–45 ka debris avalanche flow of Montagne Pelée volcano, Martinique: from volcano flank collapse to submarine emplacement. Nat. Hazards 87, 1189–1222. https://doi.org/10.1007/s11069-017-2815-5

Brunetti, M.T., Guzzetti, F., Cardinali, M., Fiorucci, F., Santangelo, M., Mancinelli, P., Komatsu, G., Borselli, L., 2014. Analysis of a new geomorphological inventory of landslides in Valles Marineris, Mars. Earth Planet. Sci. Lett. 405, 156–168. https://doi.org/10.1016/j.epsl.2014.08.025

Butcher, F.E.G., Balme, M.R., Gallagher, C., Arnold, N.S., Conway, S.J., Hagermann, A., Lewis, S.R., 2017. Recent Basal Melting of a Mid-Latitude Glacier on Mars. J. Geophys. Res. Planets 122, 2445–2468. https://doi.org/10.1002/2017JE005434

Carter, J., Poulet, F., Bibring, J.-P., Mangold, N., Murchie, S., 2013. Hydrous minerals on Mars as seen by the CRISM and OMEGA imaging spectrometers: Updated global view. J. Geophys. Res. Planets 118, 831–858. https://doi.org/10.1029/2012JE004145

Chandler, R.J., 1972. Periglacial mudslides in Vestspitsbergen and their bearing on the origin of fossil 'solifluction' shears in low angled clay slopes. Q. J. Eng. Geol. Hydrogeol. 5, 223–241. https://doi.org/10.1144/GSL.QJEG.1972.005.03.02

Chen, R.-F., Chang, K.-J., Angelier, J., Chan, Y.-C., Deffontaines, B., Lee, C.-T., Lin, M.-L., 2006. Topographical changes revealed by high-resolution airborne LiDAR data: The 1999 Tsaoling

landslide induced by the Chi–Chi earthquake. Eng. Geol. 88, 160–172. https://doi.org/10.1016/j.enggeo.2006.09.008
Chigira, M., Wu, X., Inokuchi, T., Wang, G., 2010. Landslides induced by the 2008 Wenchuan earthquake, Sichuan, China. Geomorphology 118, 225–238. https://doi.org/10.1016/j.geomorph.2010.01.003
Coleman, N.M., Dinwiddie, C.L., Baker, V.R., 2007. Evidence that floodwaters filled and overflowed Capri Chasma, Mars. Geophys. Res. Lett. 34. https://doi.org/10.1029/2006GL028872
Comegna, L., Picarelli, L., Urciuoli, G., 2007. The mechanics of mudslides as a cyclic undrained–drained process. Landslides 4, 217–232. https://doi.org/10.1007/s10346-007-0083-2
Conway, S.J., Balme, M.R., 2014. Decameter thick remnant glacial ice deposits on Mars. Geophys. Res. Lett. 41, 5402–5409. https://doi.org/10.1002/2014GL060314
Coquin, J., Mercier, D., Bourgeois, O., Decaulne, A., 2019. A paraglacial rock-slope failure origin for cirques: a case study from Northern Iceland. Géomorphologie Relief Process. Environ. 25, 117–136. https://doi.org/10.4000/geomorphologie.13057
Corominas, J., 1994. Evidence of basal erosion and shearing as mechanisms contributing the development of lateral ridges in mudslides, flow-slides, and other flow-like gravitational movements 26.
Costard, F., Forget, F., Mangold, N., Peulvast, J.P., 2002. Formation of Recent Martian Debris Flows by Melting of Near-Surface Ground Ice at High Obliquity. Science 295, 110–113. https://doi.org/10.1126/science.1066698
Crosta, G.B., Frattini, P., Valbuzzi, E., De Blasio, F.V., 2018. Introducing a New Inventory of Large Martian Landslides. Earth Space Sci. 5, 89–119. https://doi.org/10.1002/2017EA000324
De Blasio, F.V., 2011. Landslides in Valles Marineris (Mars): A possible role of basal lubrication by sub-surface ice. Planet. Space Sci. 59, 1384–1392. https://doi.org/10.1016/j.pss.2011.04.015
de Haas, T., Conway, S.J., Krautblatter, M., 2015. Recent (Late Amazonian) enhanced backweathering rates on Mars: Paracratering evidence from gully alcoves. J. Geophys. Res. Planets 120, 2169–2189. https://doi.org/10.1002/2015JE004915
de Haas, T., Hauber, E., Kleinhans, M.G., 2013. Local late Amazonian boulder breakdown and denudation rate on Mars. Geophys. Res. Lett. 40, 3527–3531. https://doi.org/10.1002/grl.50726
Delannay, R., Valance, A., Mangeney, A., Roche, O., Richard, P., 2017. Granular and particle-laden flows: from laboratory experiments to field observations. J. Phys. Appl. Phys. 50, 053001. https://doi.org/10.1088/1361-6463/50/5/053001
Ehlmann, B.L., Mustard, J.F., Murchie, S.L., Bibring, J.-P., Meunier, A., Fraeman, A.A., Langevin, Y., 2011. Subsurface water and clay mineral formation during the early history of Mars. Nature 479, 53–60. https://doi.org/10.1038/nature10582
Ehlmann, B.L., Mustard, J.F., Swayze, G.A., Clark, R.N., Bishop, J.L., Poulet, F., Des Marais, D.J., Roach, L.H., Milliken, R.E., Wray, J.J., Barnouin-Jha, O., Murchie, S.L., 2009. Identification of hydrated silicate minerals on Mars using MRO-CRISM: Geologic context near Nili Fossae and implications for aqueous alteration. J. Geophys. Res. 114, E00D08. https://doi.org/10.1029/2009JE003339
Fassett, C.I., Head, J.W., 2005. Fluvial sedimentary deposits on Mars: Ancient deltas in a crater lake in the Nili Fossae region. Geophys. Res. Lett. 32, n/a-n/a. https://doi.org/10.1029/2005GL023456
Favreau, P., Mangeney, A., Lucas, A., Crosta, G., Bouchut, F., 2010. Numerical modeling of landquakes: landslide and seismic waves. Geophys. Res. Lett. 37, n/a-n/a. https://doi.org/10.1029/2010GL043512
Félix, G., Thomas, N., 2004. Relation between dry granular flow regimes and morphology of deposits: formation of levées in pyroclastic deposits. Earth Planet. Sci. Lett. 221, 197–213. https://doi.org/10.1016/S0012-821X(04)00111-6
Fernandez-Nieto, E.D., Garres-Diaz, J., Mangeney, A., Narbona-Reina, G., 2016. A multilayer shallow model for dry granular flows with the mu(I) -rheology: application to granular collapse on erodible beds. J. Fluid Mech. 643–681.

Gallagher, C., Balme, M., 2015. Eskers in a complete, wet-based glacial system in the Phlegra Montes region, Mars. Earth Planet. Sci. Lett. 431, 96–109. https://doi.org/10.1016/j.epsl.2015.09.023
Gaudin, A., Dehouck, E., Mangold, N., 2011. Evidence for weathering on early Mars from a comparison with terrestrial weathering profiles. Icarus 216, 257–268. https://doi.org/10.1016/j.icarus.2011.09.004
Giardini, D., Lognonné, P., Banerdt, W.B., Pike, W.T., Christensen, U., Ceylan, S., Clinton, J.F., van Driel, M., Stähler, S.C., Böse, M., Garcia, R.F., Khan, A., Panning, M., Perrin, C., Banfield, D., Beucler, E., Charalambous, C., Euchner, F., Horleston, A., Jacob, A., Kawamura, T., Kedar, S., Mainsant, G., Scholz, J.-R., Smrekar, S.E., Spiga, A., Agard, C., Antonangeli, D., Barkaoui, S., Barrett, E., Combes, P., Conejero, V., Daubar, I., Drilleau, M., Ferrier, C., Gabsi, T., Gudkova, T., Hurst, K., Karakostas, F., King, S., Knapmeyer, M., Knapmeyer-Endrun, B., Llorca-Cejudo, R., Lucas, A., Luno, L., Margerin, L., McClean, J.B., Mimoun, D., Murdoch, N., Nimmo, F., Nonon, M., Pardo, C., Rivoldini, A., Manfredi, J.A.R., Samuel, H., Schimmel, M., Stott, A.E., Stutzmann, E., Teanby, N., Warren, T., Weber, R.C., Wieczorek, M., Yana, C., 2020. The seismicity of Mars. Nat. Geosci. 13, 205–212. https://doi.org/10.1038/s41561-020-0539-8
Gray, N., 2014. Erosion-deposition waves in shallow granular free-surface flows.
Grindrod, P.M., Warner, N.H., 2014. Erosion rate and previous extent of interior layered deposits on Mars revealed by obstructed landslides. Geology 42, 795–798. https://doi.org/10.1130/G35790.1
Hartmann, W.K., 2005. Martian cratering 8: Isochron refinement and the chronology of Mars. Icarus 174, 294–320. https://doi.org/10.1016/j.icarus.2004.11.023
Head, J.W., Mustard, J.F., Kreslavsky, M.A., Milliken, R.E., Marchant, D.R., 2003. Recent ice ages on Mars. Nature 426, 797–802. https://doi.org/10.1038/nature02114
Hildenbrand, A., Gillot, P.-Y., Bonneville, A., 2006. Offshore evidence for a huge landslide of the northern flank of Tahiti-Nui (French Polynesia): Tahiti-Nui landslide. Geochem. Geophys. Geosystems 7, n/a-n/a. https://doi.org/10.1029/2005GC001003
Jessop, D.E., Kelfoun, K., Labazuy, P., Mangeney, A., Roche, O., Tillier, J.-L., Trouillet, M., Thibault, G., 2012. LiDAR derived morphology of the 1993 Lascar pyroclastic flow deposits, and implication for flow dynamics and rheology - ScienceDirect.
Johnson, B.C., Campbell, C.S., 2017. Drop Height and Volume Control the Mobility of Long-Runout Landslides on the Earth and Mars. Geophys. Res. Lett. 44, 12,091-12,097. https://doi.org/10.1002/2017GL076113
Kneissl, T., van Gasselt, S., Neukum, G., 2011. Map-projection-independent crater size-frequency determination in GIS environments—New software tool for ArcGIS. Planet. Space Sci. 59, 1243–1254. https://doi.org/10.1016/j.pss.2010.03.015
Kraal, E.R., Wong, M.P., Grosfils, E.B., Gilmore, M.S., Kozak, S.J., Reinen, L.A., 1998. The Origin and Modification of a Trough in the Nili Fossae, Mars 3.
Kreslavsky, M.A., Head, J.W., Marchant, D.R., 2008. Periods of active permafrost layer formation during the geological history of Mars: Implications for circum-polar and mid-latitude surface processes. Planet. Space Sci., Mars Polar Processes: Atmosphere-Surface Interactions 56, 289–302. https://doi.org/10.1016/j.pss.2006.02.010
Laskar, J., Correia, A.C.M., Gastineau, M., Joutel, F., Levrard, B., Robutel, P., 2004. Long term evolution and chaotic diffusion of the insolation quantities of Mars. Icarus 170, 343–364. https://doi.org/10.1016/j.icarus.2004.04.005
Legros, F., 2002. The mobility of long-runout landslides. Eng. Geol. 63, 301–331. https://doi.org/10.1016/S0013-7952(01)00090-4
Levy, C., Mangeney, A., Bonilla, F., Hibert, C., Calder, E.S., Smith, P.J., 2015. Friction weakening in granular flows deduced from seismic records at the Soufrière Hills Volcano, Montserrat. J. Geophys. Res. Solid Earth 120, 7536–7557. https://doi.org/10.1002/2015JB012151
Lognonné, P., Banerdt, W.B., Giardini, D., Pike, W.T., Christensen, U., Laudet, P., de Raucourt, S., Zweifel, P., Calcutt, S., Bierwirth, M., Hurst, K.J., Ijpelaan, F., Umland, J.W., Llorca-Cejudo, R., Larson, S.A., Garcia, R.F., Kedar, S., Knapmeyer-Endrun, B., Mimoun, D., Mocquet, A., Panning,

M.P., Weber, R.C., Sylvestre-Baron, A., Pont, G., Verdier, N., Kerjean, L., Facto, L.J., Gharakanian, V., Feldman, J.E., Hoffman, T.L., Klein, D.B., Klein, K., Onufer, N.P., Paredes-Garcia, J., Petkov, M.P., Willis, J.R., Smrekar, S.E., Drilleau, M., Gabsi, T., Nebut, T., Robert, O., Tillier, S., Moreau, C., Parise, M., Aveni, G., Ben Charef, S., Bennour, Y., Camus, T., Dandonneau, P.A., Desfoux, C., Lecomte, B., Pot, O., Revuz, P., Mance, D., tenPierick, J., Bowles, N.E., Charalambous, C., Delahunty, A.K., Hurley, J., Irshad, R., Liu, H., Mukherjee, A.G., Standley, I.M., Stott, A.E., Temple, J., Warren, T., Eberhardt, M., Kramer, A., Kühne, W., Miettinen, E.-P., Monecke, M., Aicardi, C., André, M., Baroukh, J., Borrien, A., Bouisset, A., Boutte, P., Brethomé, K., Brysbaert, C., Carlier, T., Deleuze, M., Desmarres, J.M., Dilhan, D., Doucet, C., Faye, D., Faye-Refalo, N., Gonzalez, R., Imbert, C., Larigauderie, C., Locatelli, E., Luno, L., Meyer, J.-R., Mialhe, F., Mouret, J.M., Nonon, M., Pahn, Y., Paillet, A., Pasquier, P., Perez, G., Perez, R., Perrin, L., Pouilloux, B., Rosak, A., Savin de Larclause, I., Sicre, J., Sodki, M., Toulemont, N., Vella, B., Yana, C., Alibay, F., Avalos, O.M., Balzer, M.A., Bhandari, P., Blanco, E., Bone, B.D., Bousman, J.C., Bruneau, P., Calef, F.J., Calvet, R.J., D'Agostino, S.A., de los Santos, G., Deen, R.G., Denise, R.W., Ervin, J., Ferraro, N.W., Gengl, H.E., Grinblat, F., Hernandez, D., Hetzel, M., Johnson, M.E., Khachikyan, L., Lin, J.Y., Madzunkov, S.M., Marshall, S.L., Mikellides, I.G., Miller, E.A., Raff, W., Singer, J.E., Sunday, C.M., Villalvazo, J.F., Wallace, M.C., Banfield, D., Rodriguez-Manfredi, J.A., Russell, C.T., Trebi-Ollennu, A., Maki, J.N., Beucler, E., Böse, M., Bonjour, C., Berenguer, J.L., Ceylan, S., Clinton, J., Conejero, V., Daubar, I., Dehant, V., Delage, P., Euchner, F., Estève, I., Fayon, L., Ferraioli, L., Johnson, C.L., Gagnepain-Beyneix, J., Golombek, M., Khan, A., Kawamura, T., Kenda, B., Labrot, P., Murdoch, N., Pardo, C., Perrin, C., Pou, L., Sauron, A., Savoie, D., Stähler, S., Stutzmann, E., Teanby, N.A., Tromp, J., van Driel, M., Wieczorek, M., Widmer-Schnidrig, R., Wookey, J., 2019. SEIS: Insight's Seismic Experiment for Internal Structure of Mars. Space Sci. Rev. 215, 12. https://doi.org/10.1007/s11214-018-0574-6

Lucas, A., Mangeney, A., 2007. Mobility and topographic effects for large Valles Marineris landslides on Mars. Geophys. Res. Lett. 34. https://doi.org/10.1029/2007GL029835

Lucas, A., Mangeney, A., Ampuero, J.P., 2014. Frictional velocity-weakening in landslides on Earth and on other planetary bodies. Nat. Commun. 5. https://doi.org/10.1038/ncomms4417

Lucas, A., Mangeney, A., Bouchut, F., Bristeau, M.O., Mège, D., 2007. Benchmarking exercises for granular flows, in: Unpublished. https://doi.org/10.13140/rg.2.1.3945.0088

Lucas, A., Mangeney, A., Mège, D., Bouchut, F., 2011. Influence of the scar geometry on landslide dynamics and deposits: Application to Martian landslides. J. Geophys. Res. 116. https://doi.org/10.1029/2011JE003803

Lucchitta, B.K., 1979. Landslides in Valles Marineris, Mars. J. Geophys. Res. 84, 8097. https://doi.org/10.1029/JB084iB14p08097

Magnarini, G., Mitchell, T.M., Grindrod, P.M., Goren, L., Schmitt, H.H., 2019. Longitudinal ridges imparted by high-speed granular flow mechanisms in martian landslides. Nat. Commun. 10, 1–7. https://doi.org/10.1038/s41467-019-12734-0

Malin, M.C., Bell, J.F., Cantor, B.A., Caplinger, M.A., Calvin, W.M., Clancy, R.T., Edgett, K.S., Edwards, L., Haberle, R.M., James, P.B., Lee, S.W., Ravine, M.A., Thomas, P.C., Wolff, M.J., 2007. Context Camera Investigation on board the Mars Reconnaissance Orbiter. J. Geophys. Res. 112, E05S04. https://doi.org/10.1029/2006JE002808

Mangeney, A., Bouchut, F., Thomas, N., Vilotte, J.P., Bristeau, M.O., 2007. Numerical modeling of self-channeling granular flows and of their levee-channel deposits. J. Geophys. Res. Earth Surf. 112. https://doi.org/10.1029/2006JF000469

Mangeney, A., Roche, O., Hungr, O., Mangold, N., Faccanoni, G., Lucas, A., 2010. Erosion and mobility in granular collapse over sloping beds. J. Geophys. Res. Earth Surf. 115. https://doi.org/10.1029/2009JF001462

Mangeney-Castelnau, A., Bouchut, F., Vilotte, J.P., Lajeunesse, E., Aubertin, A., Pirulli, M., 2005. On the use of Saint Venant equations to simulate the spreading of a granular mass. J. Geophys. Res. Solid Earth 110. https://doi.org/10.1029/2004JB003161

Mangold, N., Mangeney, A., Migeon, V., Ansan, V., Lucas, A., Baratoux, D., Bouchut, F., 2010. Sinuous gullies on Mars: Frequency, distribution, and implications for flow properties. J. Geophys. Res. 115. https://doi.org/10.1029/2009JE003540

Mangold, N., Poulet, F., Mustard, J.F., Bibring, J.-P., Gondet, B., Langevin, Y., Ansan, V., Masson, Ph., Fassett, C., Head, J.W., Hoffmann, H., Neukum, G., 2007. Mineralogy of the Nili Fossae region with OMEGA/Mars Express data: 2. Aqueous alteration of the crust: MINERALOGY OF THE NILI FOSSAE REGION, 2. J. Geophys. Res. Planets 112. https://doi.org/10.1029/2006JE002835

Marc, O., Hovius, N., Meunier, P., Uchida, T., Hayashi, S., 2015. Transient changes of landslide rates after earthquakes. Geology 43, 883–886. https://doi.org/10.1130/G36961.1

Masson, D.G., Watts, A.B., Gee, M.J.R., Urgeles, R., Mitchell, N.C., Le Bas, T.P., Canals, M., 2002. Slope failures on the flanks of the western Canary Islands. Earth-Sci. Rev. 57, 1–35. https://doi.org/10.1016/S0012-8252(01)00069-1

McEwen, A.S., 1989. Mobility of large rock avalanches: Evidence from Valles Marineris, Mars. Geology 17, 1111–1114. https://doi.org/10.1130/0091-7613(1989)017<1111:MOLRAE>2.3.CO;2

McEwen, A.S., Eliason, E.M., Bergstrom, J.W., Bridges, N.T., Hansen, C.J., Delamere, W.A., Grant, J.A., Gulick, V.C., Herkenhoff, K.E., Keszthelyi, L., Kirk, R.L., Mellon, M.T., Squyres, S.W., Thomas, N., Weitz, C.M., 2007. Mars Reconnaissance Orbiter's High Resolution Imaging Science Experiment (HiRISE). J. Geophys. Res. Planets 112. https://doi.org/10.1029/2005JE002605

McSaveney, M., Davies, T., 2007. Rockslides and Their Motion, in: Sassa, K., Fukuoka, H., Wang, F., Wang, G. (Eds.), Progress in Landslide Science. Springer Berlin Heidelberg, Berlin, Heidelberg, pp. 113–133. https://doi.org/10.1007/978-3-540-70965-7_8

Mellon, M.T., Phillips, R.J., 2001. Recent gullies on Mars and the source of liquid water. J. Geophys. Res. Planets 106, 23165–23179. https://doi.org/10.1029/2000JE001424

Meunier, P., Hovius, N., Haines, A.J., 2007. Regional patterns of earthquake-triggered landslides and their relation to ground motion. Geophys. Res. Lett. 34. https://doi.org/10.1029/2007GL031337

Michael, G.G., 2013. Planetary surface dating from crater size–frequency distribution measurements: Multiple resurfacing episodes and differential isochron fitting. Icarus 226, 885–890. https://doi.org/10.1016/j.icarus.2013.07.004

Michael, G.G., Kneissl, T., Neesemann, A., 2016. Planetary surface dating from crater size-frequency distribution measurements: Poisson timing analysis. Icarus 277, 279–285. https://doi.org/10.1016/j.icarus.2016.05.019

Michael, G.G., Neukum, G., 2010. Planetary surface dating from crater size–frequency distribution measurements: Partial resurfacing events and statistical age uncertainty. Earth Planet. Sci. Lett. 294, 223–229. https://doi.org/10.1016/j.epsl.2009.12.041

Michael, G.G., Platz, T., Kneissl, T., Schmedemann, N., 2012. Planetary surface dating from crater size–frequency distribution measurements: Spatial randomness and clustering. Icarus 218, 169–177. https://doi.org/10.1016/j.icarus.2011.11.033

Michalski, J., Poulet, F., Bibring, J.-P., Mangold, N., 2010. Analysis of phyllosilicate deposits in the Nili Fossae region of Mars: Comparison of TES and OMEGA data. Icarus 206, 269–289. https://doi.org/10.1016/j.icarus.2009.09.006

Moratto, Z.M., Michael J. Broxton, Ross A. Beyer, Mike Lundy, Kyle Husmann, 2010. Ames Stereo Pipeline, NASA's Open Source Automated Stereogrammetry Software. 41st Lunar and Planetary Science Conference.

Moretti, L., Allstadt, K., Mangeney, A., Capdeville, Y., Stutzmann, E., Bouchut, F., 2015. Numerical modeling of the Mount Meager landslide constrained by its force history derived from seismic data. J. Geophys. Res. Solid Earth 120, 2579–2599. https://doi.org/10.1002/2014JB011426

Moretti, L., Mangeney, A., Capdeville, Y., Stutzmann, E., Huggel, C., Schneider, D., Bouchut, F., 2012. Numerical modeling of the Mount Steller landslide flow history and of the generated long period seismic waves: landquake modeling. Geophys. Res. Lett. 39, n/a-n/a. https://doi.org/10.1029/2012GL052511

Moretti, L., Mangeney, A., Walter, F., Capdeville, Y., Bodin, T., Stutzmann, E., Le Friant, A., 2020. Constraining landslide characteristics with Bayesian inversion of field and seismic data. Geophys. J. Int. 221, 1341–1348. https://doi.org/10.1093/gji/ggaa056

Murchie, S., Arvidson, R., Bedini, P., Beisser, K., Bibring, J.-P., Bishop, J., Boldt, J., Cavender, P., Choo, T., Clancy, R.T., Darlington, E.H., Des Marais, D., Espiritu, R., Fort, D., Green, R., Guinness, E., Hayes, J., Hash, C., Heffernan, K., Hemmler, J., Heyler, G., Humm, D., Hutcheson, J., Izenberg, N., Lee, R., Lees, J., Lohr, D., Malaret, E., Martin, T., McGovern, J.A., McGuire, P., Morris, R., Mustard, J., Pelkey, S., Rhodes, E., Robinson, M., Roush, T., Schaefer, E., Seagrave, G., Seelos, F., Silverglate, P., Slavney, S., Smith, M., Shyong, W.-J., Strohbehn, K., Taylor, H., Thompson, P., Tossman, B., Wirzburger, M., Wolff, M., 2007. Compact Reconnaissance Imaging Spectrometer for Mars (CRISM) on Mars Reconnaissance Orbiter (MRO). J. Geophys. Res. 112, E05S03. https://doi.org/10.1029/2006JE002682

Mustard, J.F., Cooper, C.D., Rifkin, M.K., 2001. Evidence for recent climate change on Mars from the identification of youthful near-surface ground ice. Nature 412, 411–414. https://doi.org/10.1038/35086515

Mustard, J.F., Poulet, F., Head, J.W., Mangold, N., Bibring, J.-P., Pelkey, S.M., Fassett, C.I., Langevin, Y., Neukum, G., 2007. Mineralogy of the Nili Fossae region with OMEGA/Mars Express data: 1. Ancient impact melt in the Isidis Basin and implications for the transition from the Noachian to Hesperian. J. Geophys. Res. Planets 112. https://doi.org/10.1029/2006JE002834

Nereson, A.L., Finnegan, N.J., 2015. Earthflow yield strength constrained by lateral levee morphology. AGU Fall Meet. Abstr. 2015, EP41C-0943.

Neukum, G., Jaumann, R., 2004. HRSC: the High Resolution Stereo Camera of Mars Express 1240, 17–35.

Niu, F., Luo, J., Lin, Z., Fang, J., Liu, M., 2015. Thaw-induced slope failures and stability analyses in permafrost regions of the Qinghai-Tibet Plateau, China. Landslides 13. https://doi.org/10.1007/s10346-014-0545-2

Pajola, M., Rossato, S., Baratti, E., Mangili, C., Mancarella, F., McBride, K., Coradini, M., 2016. The Simud–Tiu Valles hydrologic system: A multidisciplinary study of a possible site for future Mars on-site exploration. Icarus 268, 355–381. https://doi.org/10.1016/j.icarus.2015.12.049

Parise, M., 2003. Observation of surface features on an active landslide, and implications for understanding its history of movement. Nat. Hazards Earth Syst. Sci. 3, 569–580. https://doi.org/10.5194/nhess-3-569-2003

Peruzzetto, M., Komorowski, J.-C., Le Friant, A., Rosas-Carbajal, M., Mangeney, A., Legendre, Y., 2019. Modeling of partial dome collapse of La Soufrière of Guadeloupe volcano: implications for hazard assessment and monitoring. Sci. Rep. 9, 1–15. https://doi.org/10.1038/s41598-019-49507-0

Porter, C., Morin, P., Howat, I., Noh, M.-J., Bates, B., Peterman, K., Keesey, S., Schlenk, M., Gardiner, J., Tomko, K., Willis, M., Kelleher, C., Cloutier, M., Husby, E., Foga, S., Nakamura, H., Platson, M., Wethington, M., Williamson, C., Bauer, G., Enos, J., Arnold, G., Kramer, W., Becker, P., Doshi, A., D'Souza, C., Cummens, P., Laurier, F., Bojesen, M., 2018. ArcticDEM. https://doi.org/10.7910/DVN/OHHUKH

Poulet, F., Bibring, J.-P., Mustard, J.F., Gendrin, A., Mangold, N., Langevin, Y., Arvidson, R.E., Gondet, B., Gomez, C., 2005. Phyllosilicates on Mars and implications for early martian climate. Nature 438, 623. https://doi.org/10.1038/nature04274

Pouliquen, O., Forterre, Y., 2002. Friction law for dense granular flows: application to the motion of a mass down a rough inclined plane. J. Fluid Mech. 453, 133–151. https://doi.org/10.1017/S0022112001006796

Quantin, C., Allemand, P., Delacourt, C., 2004a. Morphology and geometry of Valles Marineris landslides. Planet. Space Sci. 52, 1011–1022. https://doi.org/10.1016/j.pss.2004.07.016

Quantin, C., Allemand, P., Mangold, N., Delacourt, C., 2004b. Ages of Valles Marineris (Mars) landslides and implications for canyon history. Icarus 172, 555–572. https://doi.org/10.1016/j.icarus.2004.06.013

Rapp, A., 1960. Recent Development of Mountain Slopes in Kärkevagge and Surroundings, Northern Scandinavia. Geogr. Ann. 42, 65–200. https://doi.org/10.1080/20014422.1960.11880942

Rocha, F.M., Johnson, C.G., Gray, J.M.N.T., 2019. Self-channelisation and levee formation in monodisperse granular flows. J. Fluid Mech. 876, 591–641. https://doi.org/10.1017/jfm.2019.518

Sæmundsson, Þ., Morino, C., Helgason, J.K., Conway, S.J., Pétursson, H.G., 2018. The triggering factors of the Móafellshyrna debris slide in northern Iceland: Intense precipitation, earthquake activity and thawing of mountain permafrost. Sci. Total Environ. 621, 1163–1175. https://doi.org/10.1016/j.scitotenv.2017.10.111

Sassa, K., Fukuoka, H., Wang, F., Wang, G., 2007. Landslides Induced by a Combined Effect of Earthquake and Rainfall, in: Sassa, K., Fukuoka, H., Wang, F., Wang, G. (Eds.), Progress in Landslide Science. Springer, Berlin, Heidelberg, pp. 193–207. https://doi.org/10.1007/978-3-540-70965-7_14

Schultz, R.A., 2002. Stability of rock slopes in Valles Marineris, Mars. Geophys. Res. Lett. 29, 38-1-38–4. https://doi.org/10.1029/2002GL015728

Schultz, R.A., 2000. Localization of bedding plane slip and backthrust faults above blind thrust faults: Keys to wrinkle ridge structure. J. Geophys. Res. Planets 105, 12035–12052. https://doi.org/10.1029/1999JE001212

Sepúlveda, S.A., Serey, A., Lara, M., Pavez, A., Rebolledo, S., 2010. Landslides induced by the April 2007 Aysén Fjord earthquake, Chilean Patagonia. Landslides 7, 483–492. https://doi.org/10.1007/s10346-010-0203-2

Shaller, P.J., 1991. Analysis and implications of large Martian and terrestrial landslides. California Institute of Technology.

Sharp, R.P., 1973. Mars: Troughed terrain. J. Geophys. Res. 1896-1977 78, 4063–4072. https://doi.org/10.1029/JB078i020p04063

Shea, T., van Wyk de Vries, B., 2008. Structural analysis and analogue modeling of the kinematics and dynamics of rockslide avalanches. Geosphere 4, 657. https://doi.org/10.1130/GES00131.1

Smith, D.E., Zuber, M.T., Frey, H.V., Garvin, J.B., Head, J.W., Muhleman, D.O., Pettengill, G.H., Phillips, R.J., Solomon, S.C., Zwally, H.J., Banerdt, W.B., Duxbury, T.C., Golombek, M.P., Lemoine, F.G., Neumann, G.A., Rowlands, D.D., Aharonson, O., Ford, P.G., Ivanov, A.B., Johnson, C.L., McGovern, P.J., Abshire, J.B., Afzal, R.S., Sun, X., 2001. Mars Orbiter Laser Altimeter: Experiment summary after the first year of global mapping of Mars. J. Geophys. Res. Planets 106, 23689–23722. https://doi.org/10.1029/2000JE001364

Soukhovitskaya, V., Manga, M., 2006. Martian landslides in Valles Marineris: Wet or dry? Icarus 180, 348–352. https://doi.org/10.1016/j.icarus.2005.09.008

Strecker, M.R., Fauque, L., 1988. Large rock avalanche deposits (Sturzströme, sturzstroms) at Sierra Aconquija, northern Sierras Pampeanas, Argentina. https://doi.org/10.5169/seals-166195

Tanaka, K.L., Skinner, J.A., Dohm, J.M., Irwin, R.P., Kolb, E.J., Fortezzo, C.M., Platz, T., Michael, G.G., Hare, T.M., 2014. Scientific Investigations Map (Scientific Investigations Map).

Tanaka, K.L., Skinner, J.A., Hare, T.M., Joyal, T., Wenker, A., 2003. Resurfacing history of the northern plains of Mars based on geologic mapping of Mars Global Surveyor data. J. Geophys. Res. Planets 108. https://doi.org/10.1029/2002JE001908

Teanby, N.A., Wookey, J., 2011. Seismic detection of meteorite impacts on Mars. Phys. Earth Planet. Inter. 186, 70–80. https://doi.org/10.1016/j.pepi.2011.03.004

Tesson, P.-A., Conway, S.J., Mangold, N., Ciazela, J., Lewis, S.R., Mège, D., 2019. Evidence for thermal fatigue on Mars from rockfall patterns on impact crater slopes. Presented at the 50th Lunar and Planetary Science Conference, The Woodlands, Houston, Texas, USA.

Thomas, N., Cremonese, G., Ziethe, R., Gerber, M., Brändli, M., Bruno, G., Erismann, M., Gambicorti, L., Gerber, T., Ghose, K., Gruber, M., Gubler, P., Mischler, H., Jost, J., Piazza, D., Pommerol, A., Rieder, M., Roloff, V., Servonet, A., Trottmann, W., Uthaicharoenpong, T., Zimmermann, C., Vernani, D., Johnson, M., Pelò, E., Weigel, T., Viertl, J., De Roux, N., Lochmatter, P., Sutter, G., Casciello, A., Hausner, T., Ficai Veltroni, I., Da Deppo, V., Orleanski, P., Nowosielski, W.,

Zawistowski, T., Szalai, S., Sodor, B., Tulyakov, S., Troznai, G., Banaskiewicz, M., Bridges, J.C., Byrne, S., Debei, S., El-Maarry, M.R., Hauber, E., Hansen, C.J., Ivanov, A., Keszthelyi, L., Kirk, R., Kuzmin, R., Mangold, N., Marinangeli, L., Markiewicz, W.J., Massironi, M., McEwen, A.S., Okubo, C., Tornabene, L.L., Wajer, P., Wray, J.J., 2017. The Colour and Stereo Surface Imaging System (CaSSIS) for the ExoMars Trace Gas Orbiter. Space Sci. Rev. 212, 1897–1944. https://doi.org/10.1007/s11214-017-0421-1

Vallf-Jo, L.E., 1979. Mechanics of mudflow mobilization in low-angled clay slopes 8.

Viviano, C.E., Moersch, J.E., McSween, H.Y., 2013. Implications for early hydrothermal environments on Mars through the spectral evidence for carbonation and chloritization reactions in the Nili Fossae region. J. Geophys. Res. Planets 118, 1858–1872. https://doi.org/10.1002/jgre.20141

Walter, M., Joswig, M., 2008. Seismic monitoring of fracture processes from a creeping landslide in the Vorarlberg Alps. Geophys Res Abstr 10, 09212.

Wang, F.W., Sassa, K., Wang, G., 2002. Mechanism of a long-runout landslide triggered by the August 1998 heavy rainfall in Fukushima Prefecture, Japan. Eng. Geol. 63, 169–185. https://doi.org/10.1016/S0013-7952(01)00080-1

Warner, N.H., Gupta, S., Calef, F., Grindrod, P., Boll, N., Goddard, K., 2015. Minimum effective area for high resolution crater counting of martian terrains. Icarus 245, 198–240. https://doi.org/10.1016/j.icarus.2014.09.024

Watkins, J.A., Ehlmann, B.L., Yin, A., 2015. Long-runout landslides and the long-lasting effects of early water activity on Mars. Geology 43, 107–110. https://doi.org/10.1130/G36215.1

Wichman, R.W., Schultz, P.H., 1989. Sequence and mechanisms of deformation around the Hellas and Isidis Impact Basins on Mars. J. Geophys. Res. Solid Earth 94, 17333–17357. https://doi.org/10.1029/JB094iB12p17333

Wójcicka, N., Collins, G.S., Bastow, I.D., Teanby, N.A., Miljković, K., Rajšić, A., Daubar, I., Lognonné, P., 2020. The Seismic Moment and Seismic Efficiency of Small Impacts on Mars. J. Geophys. Res. Planets 125, e2020JE006540. https://doi.org/10.1029/2020JE006540

Yamada, M., Mangeney, A., Matsushi, Y., Matsuzawa, T., 2018. Estimation of dynamic friction and movement history of large landslides. Landslides 15, 1963–1974. https://doi.org/10.1007/s10346-018-1002-4

Yamada, M., Mangeney, A., Matsushi, Y., Moretti, L., 2016. Estimation of dynamic friction of the Akatani landslide from seismic waveform inversion and numerical simulation. Geophys. J. Int. 206, 1479–1486. https://doi.org/10.1093/gji/ggw216

Supplementary material

S1-Spectral analysis

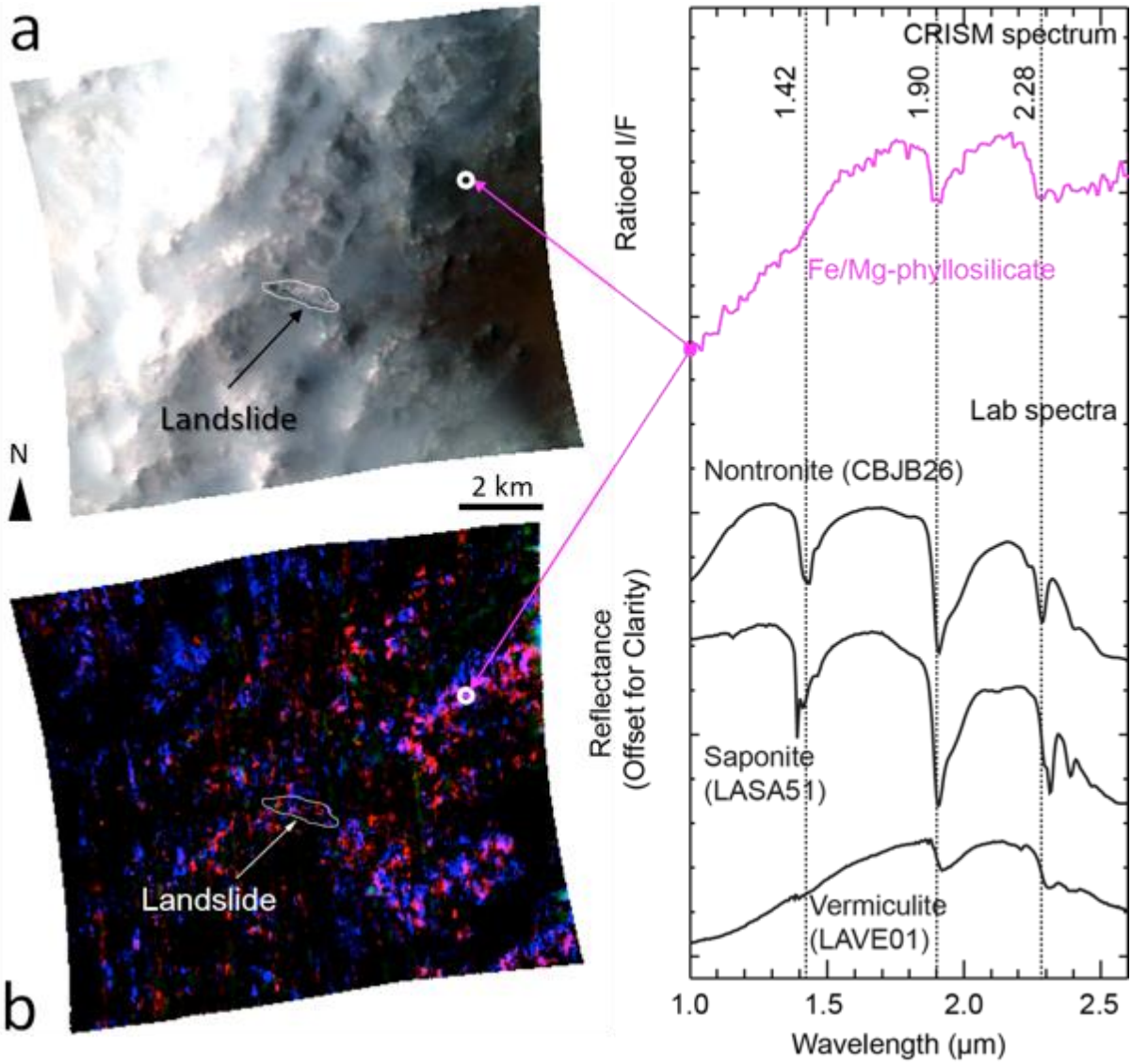

Figure S1 - Fe/Mg clays exposed along the impact crater rim in Nili Fossae region. (a) CRISM enhanced IR colour, R= 2.5 μm; G= 1.5 μm; B= 1.1 μm. (b) Spectral parameter map, R= 2.3 μm band depth (D2300); G= 2.2 μm band depth (BD2200); B= 1.9 μm band depth (BD1900R), pink colour: Fe/Mg phyllosilicates, blue colour: hydrated phase. (c) CRISM spectrum of Fe/Mg-phyllosilicate 'average' of several pixels divided by pixels of a neutral region compared to laboratory spectra (RELAB library spectra). (CRISM: HRS00024571_07_IF175S_TRR3)

The hyperspectral CRISM observation presented in Figure S1 was processed using the CAT (CRISM Analysis Toolkit; (Morgan et al., 2014)) extension for the ENVI software (Exelis VIS), which was developed by the CRISM Science Team. The spectral parameter maps were computed using the spectral parameter summary products produced by Viviano-Beck et al. (2014).

Fe-Mg-phyllosilicates (pink tones in Fig.S1b) such as nontronite, saponite, and vermiculite are observed on the bedrock along the impact crater rim and on its floor in the region where the Nilosyrtis Mensae landslide occurs. Other hydrated phase(s) are also associated with the bedrock. Either this or these hydrated phases are not phyllosilicates, or if they correspond to phyllosilicates, then the amount is too small for their diagnostic absorption band at 2.3 μm to be detected.

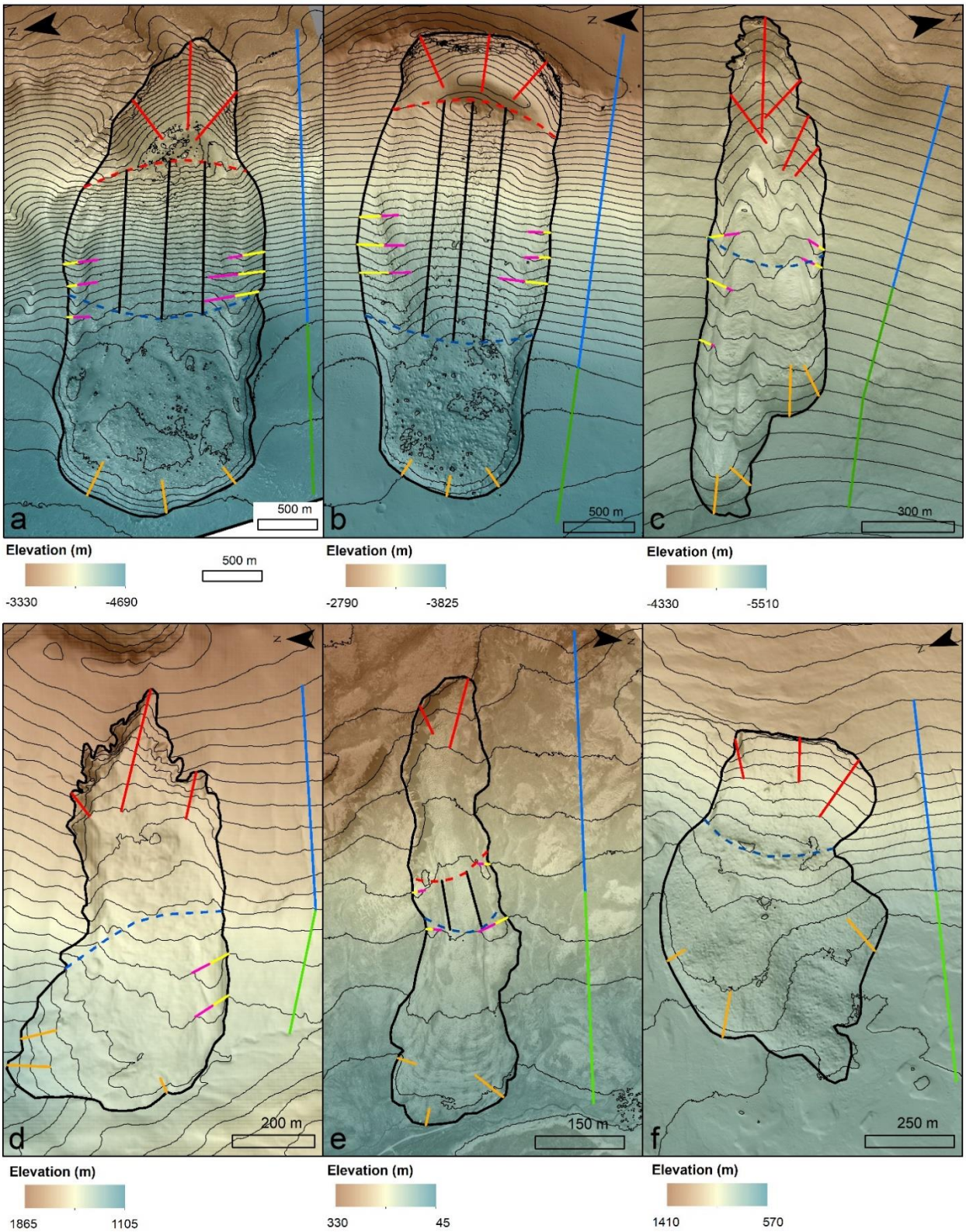

Figure S2 – Position of topographic profiles used to extract measured parameters on Mars (a) Capri Chasma; (b) Chryse Chaos and (c) Nilosyrtis Mensae and on Earth (d) Mount Rainier; (e) Hólmavík and (f) Abisko. Profiles in red, black and orange are used for the erosion zone, the transport zone and front scarp slope calculations, respectively. Profiles outside the landslide's boundary in blue and in green are used to estimate the slope angle before the landslide occurred and to estimate the slope underlying the deposit zone, respectively. Profiles in yellow and pink are used for outer and inner levee angle calculation, respectively. The dashed line in red delimits the erosion zone and the dashed line in blue delimits the deposition zone. Background images: HiRISE images for (a) ESP_035831_1760, *(b)* PSP_005701_1920 *and (c)* ESP_026781_2075; *(d)* Washington Lidar Portal hillshaded rendering, (e) Aerial image from the Land Survey of Iceland and (f) hillshaded LiDAR data from Geographical Sweden Data.

S2-Topographic profiles

On figure S2, for the three profiles placed for each levee, each cross-section line was placed by connecting with a straight line the points where a given contour line crosses the levee boundary on each side. We isolated each levee by identifying the point at which it rose from the surrounding terrain aided by the image data and extracted the elevation values at these points. We identified and extracted the elevation of the crest of the levee. For each side we calculated the slopes by taking the arctangent of the difference between the base and crest elevations divided by the distance to the crest along the profile. We extracted the maximum height for each levee by taking the maximum difference between the base and crest elevations.

S3-Grain size sensitivity tests

In order to investigate the influence of grain size in the model using the Pouliquen and Forterre's law, we performed a sensitivity test on the Capri Chasma landslide by taking grain sizes of L= 1 cm, 1 m, 5 m, 10 m and 20 m (Figure S3). The grain size influences the friction coefficients required to correctly fit the runout distance. The smaller the grain size, the smaller the friction angles must be. In addition, the smaller the grain size, the less rounded the landslide deposit front is. The decision to use L= 5 m for CCh and ChrC and L= 1 cm for Nilosyrtis Mensae is based on morphological observations of the deposition surface. On the CCh and ChrC slides, the entire deposition surface is covered with blocks larger than 5 m. This size has therefore been taken as a reference for modelling. For NM landslide, there are only a few scattered blocks of maximum 10 m in size near the toe of the deposit. Also, we have not identified any blocs of one metre or more on the main deposit it's that why we choose to take our smaller tested value of 1 cm to conduct the NM simulations.

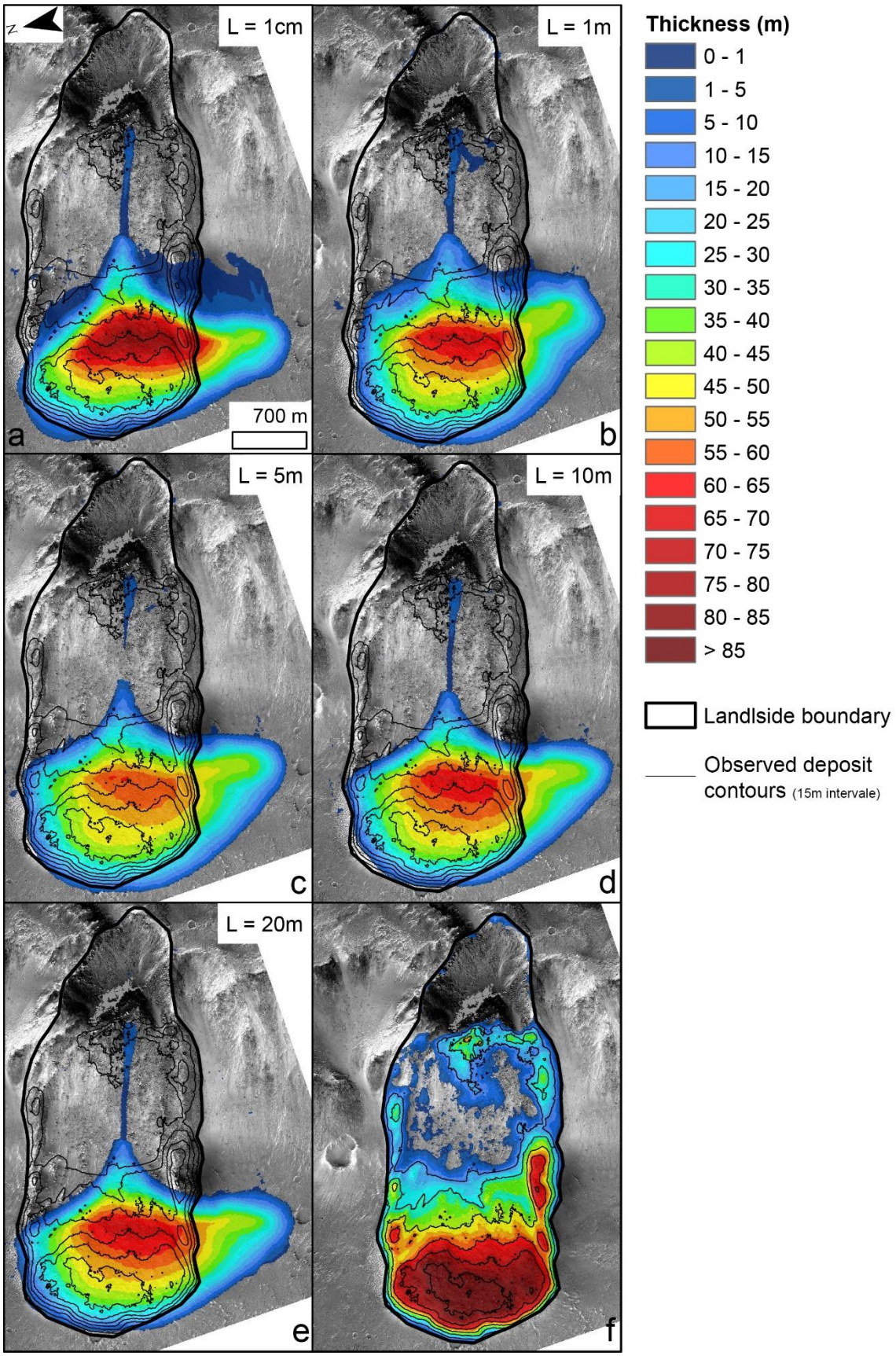

1405 *Figure S3 – Final deposit thickness maps resulting from the grain size sensitivity tests applied to Capri Chasma landslide*
1406 *simulation with grain size (L) of (a) 1 cm; (b) 1 m; (c) 5 m; (d) 10 m; (e) 20 m. (f) is the observed deposit on Mars.*

1407

S4-Topographic reconstructions

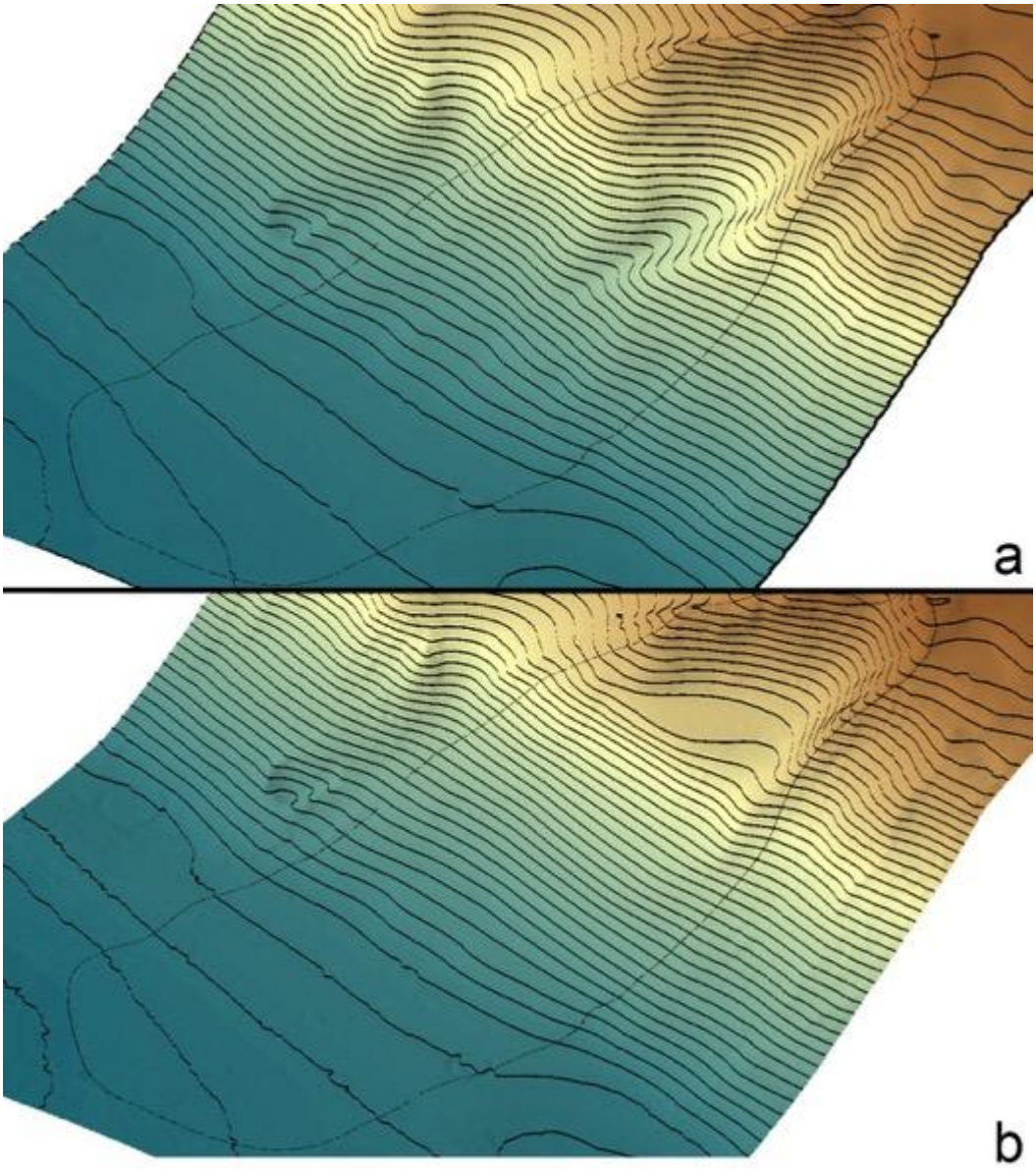

Figure S4 - 3D view of two alternate topographic reconstructions for Capri Chasma landslide, where the colourised DEM is overlain by semi-transparent hillshaded relief and 25 m interval contour lines in black. (a) Reconstruction with overdeepened areas in the erosion zone. (b) Reconstruction with a flattened base in the erosion zone.

We tested two alternate reconstructions of the initial topography of Capri Chasma landslide to assess the sensitivity of the numerical modelling to this parameter. The actual topography of the erosion zone is unknown as it is partially covered with deposits. We tested the two end members shown in Figure S4.

The reconstruction in Figure S4a includes an over-deepening at the centre of the erosion zone and in Figure S4b a flatter topographic base of the erosion zone. The results of test simulations using these two reconstructions are shown in Figures S5e for the flattened reconstruction and S5f for the overdeepened reconstruction. For the flatter topography (Fig. S5e) some of the mass is retained in the erosion zone as is observed for the real deposit, but significant mass is deflected to one side, hence we did not choose this reconstruction, as it was a poor fit for the observed deposits. For the overdeepened reconstruction (Fig. S5f), we observe almost no deposition at the base of the erosion zone and the deposit is located more centrally within the deposition zone compared to the flattened

erosion zone reconstruction. The results are almost indistinguishable from those with no overdeepened portion (Figure 11f), hence for simplicity we decided not to use this reconstruction as the presence/absence of this overdeepened section was impossible to determine.

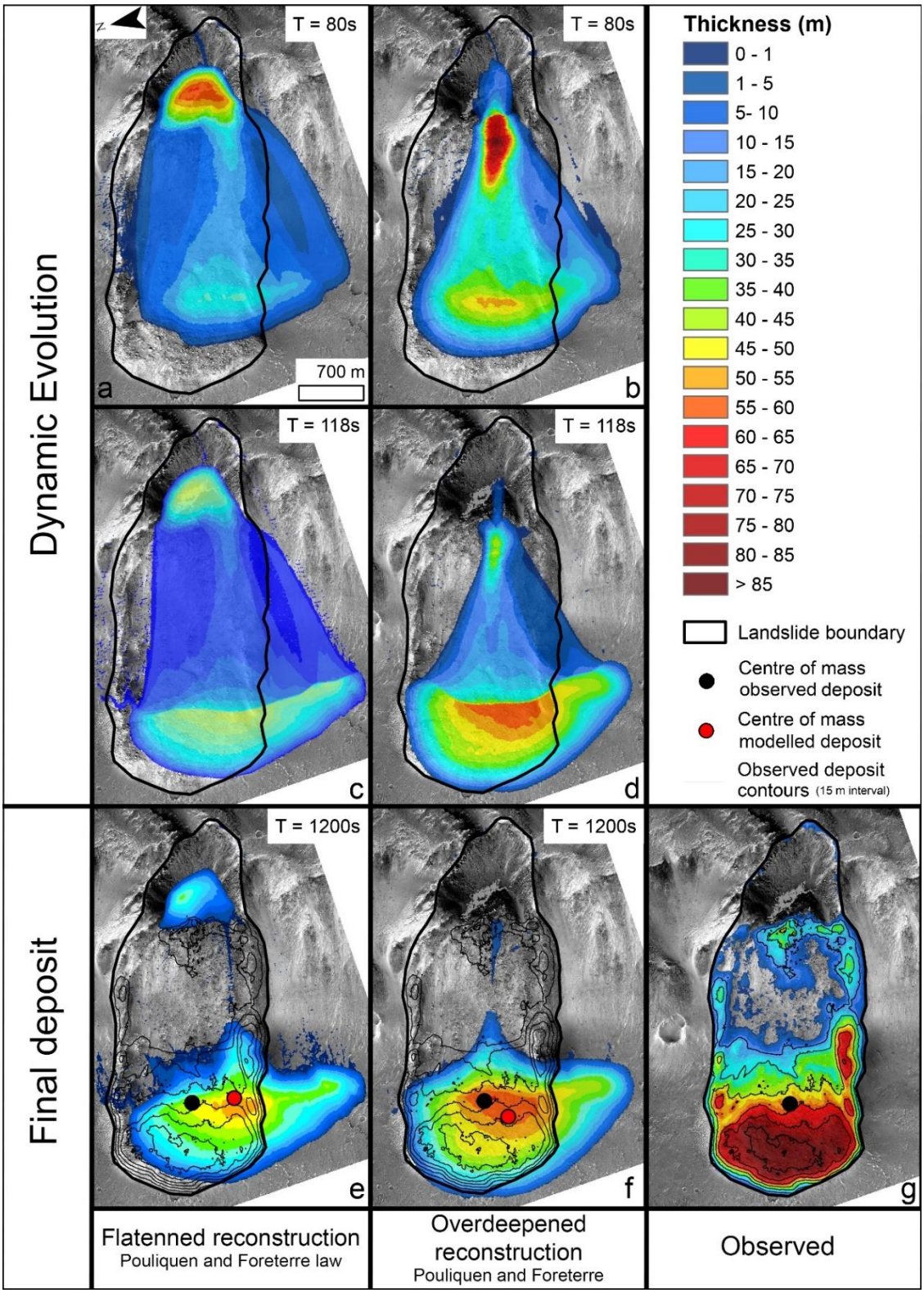

Figure S5 - Dynamic evolution of the simulation using flattened topographic reconstruction of the erosion zone (figure S4b), (a) at T=80s, (c) at T=118s and (e) at T=1200s when the flow is stabilised and using the overdeepened reconstruction (b) at T=80s, (d) at T=118s and (f) at T=1200s when the flow is stabilised compared to (g), the actual deposits. Pouliquen and Forterre's law used with angles of δ_1= 8, δ_2= 18 and δ_3= 11°.

References

Morgan, F., Seelos, F.P., Murchie, S.L., CRISM Team, 2014. CRISM Analysis Toolkit (CAT). The Johns Hopkins University.

Viviano-Beck, C.E., Seelos, F.P., Murchie, S.L., Kahn, E.G., Seelos, K.D., Taylor, H.W., Taylor, K., Ehlmann, B.L., Wiseman, S.M., Mustard, J.F., Morgan, M.F., 2014. Revised CRISM spectral parameters and summary products based on the currently detected mineral diversity on Mars. Journal of Geophysical Research: Planets 119, 1403–1431. https://doi.org/10.1002/2014JE004627